The Astrophysical Journal, 904:112 (19pp), 2020 December 1 https://doi.org/10.3847/1538-4357/abc172

Hubble Space Telescope Astrometry of the Metal-poor Visual Binary μ Cassiopeiae: Dynamical Masses, Helium Content, and Age[*]

Howard E. Bond[1,2], Gail H. Schaefer[3], Ronald L. Gilliland[1,2], and Don A. VandenBerg[4]
[1] Department of Astronomy & Astrophysics, Pennsylvania State University, University Park, PA 16802, USA; heb11@psu.edu
[2] Space Telescope Science Institute, 3700 San Martin Dr., Baltimore, MD 21218, USA
[3] The CHARA Array of Georgia State University, Mount Wilson Observatory, Mount Wilson, CA 91023, USA
[4] Department of Physics & Astronomy, University of Victoria, P.O. Box 1700 STN CSC, Victoria, BC V8W 2Y2, Canada

Received 2020 August 17; revised 2020 October 11; accepted 2020 October 13; published 2020 November 25

Abstract

μ Cassiopeiae is a nearby, high-velocity, metal-poor ([Fe/H] = -0.81) visual binary. We have used high-resolution imaging with the Hubble Space Telescope (HST), obtained over nearly two decades, to determine the period (21.568 yr) and precise orbital elements. Combining these with published ground- and space-based astrometry, we determined dynamical masses for both components of μ Cas: $0.7440 \pm 0.0122\,M_\odot$ for the G5 V primary and $0.1728 \pm 0.0035\,M_\odot$ for its faint dM companion. We detect no significant perturbations in the HST astrometry owing to a third body in the system. The primary aim of our program was to determine, with the aid of stellar models, the helium content and age of the metal-deficient primary star, μ Cas A. Although we now have a precise mass, there remain uncertainties about other parameters, including its effective temperature. Moreover, a reexamination of archival interferometric observations leads to a suspicion that the angular diameter was overestimated by a few percent. In the absolute magnitude versus color plane, μ Cas A lies slightly cooler and more luminous than the main sequence of the globular cluster 47 Tucanae; this may imply that the star has a lower helium content, and/or is older, and/or has a higher metallicity, than the cluster. Our best estimates for the helium content and age of μ Cas A are $Y = 0.255 \pm 0.014$ and 12.7 ± 2.7 Gyr—making μ Cas possibly the oldest star in the sky visible to the naked eye. Improved measurements of the absolute parallax of the system, the effective temperature of μ Cas A, and its angular diameter would provide tighter constraints.

Unified Astronomy Thesaurus concepts: Binary stars (154); Stellar evolutionary models (2046); Space astrometry (1541); Visual binary stars (1777); Stellar masses (1614)

1. μ Cassiopeiae: An Important Metal-poor Visual Binary

The nearby fifth-magnitude G5 V star μ Cassiopeiae was one of the first "high-velocity" stars to be recognized (Campbell 1901; Adams & Joy 1919; Oort 1926; Miczaika 1940; Roman 1955). With a radial velocity (RV) of -97 km s^{-1} (Agati et al. 2015, and references therein), a distance of 7.55 pc, and a proper motion of 3$''$78 yr^{-1} (the last two values from the Hipparcos mission; van Leeuwen 2007), the star has a total space motion relative to the Sun of 167 km s^{-1} and can be considered a thick-disk or possibly a halo object. Johnson & Morgan (1953), in their classical paper that introduced *UBV* photometry, noted that μ Cas lies below the main sequence (MS) in the color−absolute magnitude diagram for nearby stars with accurate distances, and that its $U - B$ index is relatively blue for its $B - V$ color. It was soon recognized that the low luminosities and ultraviolet excesses of high-velocity dwarfs are the result of low heavy-element contents. As discussed below, modern spectroscopic analyses of μ Cas give a photospheric metal abundance of about 1/6 that of the Sun ([Fe/H] $\simeq -0.8$).

Photographic positional measurements of μ Cas over a quarter of a century at the Allegheny Observatory led to the discovery that the star is an astrometric binary, showing a perturbation due to an unseen companion with an orbital period of about 23 yr (Wagman 1961; Wagman et al. 1963). An astrometric analysis of photographic plates from the Sproul Observatory, also over an interval of about a quarter century, refined the orbital period to ∼18.5 yr (Lippincott & Wyckoff 1964). Based on additional Sproul material, Lippincott (1981) updated the period again to 21.43 yr, and then Russell & Gatewood (1984) further revised the astrometric perturbation period to 22.09 yr, based on Allegheny photographic material covering 45 yr. A final analysis of all of the Sproul plates, now covering 55 yr, gave a period of 21.40 yr (Heintz & Cantor 1994).

The astrophysical importance of μ Cas was emphasized by Dennis (1965, hereafter D65). The primordial abundance of helium and the history of its increase over cosmic time due to stellar nucleosynthesis are important constraints on cosmology and Galactic evolution. However, the old stellar populations that have survived to the present epoch contain primarily cool MS stars and red giants, lacking helium lines in their spectra. D65 argued that, because of its binary nature, μ Cas offers the possibility of determining the helium content in an old, metal-poor star through an alternative approach. By measuring its dynamical mass, and thus the position of μ Cas in the mass–luminosity plane, one can infer its interior helium content using theoretical stellar models. A note of caution, however, was issued by Faulkner (1971), who noted that a useful cosmological constraint would require very precise knowledge of the dynamical masses of the binary. Haywood et al. (1992) gave an interpolation formula for the dependence of the derived helium mass fraction, *Y*, on measured mass; it shows that the inferred value of *Y* decreases by about 0.01 per increase in mass of 0.01 $M_\odot$. Thus, a meaningful constraint on the He content requires a mass of μ Cas A known to better than ∼0.01–0.02 $M_\odot$.

D65's paper inspired observers to attempt to detect the μ Cas companion—which was, however, expected to be extremely

---

[*] Based on observations with the NASA/ESA Hubble Space Telescope obtained at Space Telescope Science Institute, operated by Association of Universities for Research in Astronomy, Inc., under NASA contract NAS5-26555.

faint and difficult. D65 predicted μ Cas B to be an M dwarf with a visual magnitude difference relative to μ Cas A of ~6 to 8 mag. The anticipated angular separation, reaching a maximum in the mid-1960s and then rapidly decreasing, was a little more than one second of arc. Almost a decade passed before the first successful resolution of the pair, using stellar interferometry, was reported by Wickes & Dicke (1974); they also reference several earlier failed attempts.[5] They measured a separation of $0\farcs35$ and an optical magnitude difference of 5.5 mag. The resolution was confirmed in another interferometric observation a year later (Wickes 1975), but orbital motion had reduced the separation to only $0\farcs23$.

Accurate astrometry of this binary is close to the limit of what is possible with ground-based techniques, especially around periastron passage. Since the work in the 1970s, only a handful of additional ground-based measurements have been published, as discussed below. Drummond et al. (1995) resolved the binary in two adaptive optics observations obtained in 1994; based on the available data, they carried out an orbital solution and derived component masses of $0.742 \pm 0.059\ M_\odot$ and $0.173 \pm 0.011\ M_\odot$. Their results implied a helium content for μ Cas A of $Y = 0.24 \pm 0.07$, an uncertainty too large for a worthwhile cosmological or astrophysical constraint. Horch et al. (2015, 2019) presented speckle astrometry of the system at three epochs; they obtained a total mass of $0.906 \pm 0.023\ M_\odot$ but did not derive individual masses.

By contrast, resolution of the system is relatively easy from space, based on images taken with the Hubble Space Telescope (HST). In this paper, we report astrometry of μ Cas, obtained with HST over an interval of nearly two decades. By combining the HST data with the ground-based measurements, we derive precise orbital elements for the binary and the dynamical masses of both components. We also place limits on third bodies in the system. We then apply these results to a discussion of the helium content, age, and other properties of this important bright, old, and metal-poor star.

2. HST Observations

We began a program of HST imaging of μ Cas in 1997 and continued it until 2016, for a total of 27 epochs. Observations from 1997 to 2007 were made with the Wide Field Planetary Camera 2 (WFPC2) during 20 visits. The WFPC2 was removed from the spacecraft during the astronaut servicing mission in 2009 and replaced with the Wide Field Camera 3 (WFC3). We used the WFC3 UVIS channel for an additional seven visits to μ Cas from 2010 to 2016. Our observations of μ Cas were part of a long-term program of HST astrometry of astrophysically important visual binaries, which also included imaging of the Procyon and Sirius systems. Results for the latter two binaries have been published by Bond et al. (2015, hereafter B15) and Bond et al. (2018) for Procyon and by Bond et al. (2017, hereafter B17) for Sirius.

Table 1

HST Observing Log for μ Cas

UT Date	Data Set[a]	Exposure Time(s) (s)	No. Frames[b]	Proposal ID[c]
WFPC2/PC Frames, F953N Filter[d]				
1997 Jul 04	U42K0201M	0.3, 0.5	14	7497
1998 Jan 02	U42K0301R	0.3, 0.5	14	7497
1998 Jul 22	U42K0401R	1.0	15	7497
1999 Feb 28	U42K0901R	1.0	15	7497
1999 Aug 04	U59H0201R	1.0	15	8396
2000 Feb 01	U59H0301R	0.8	15	8396
2000 Jul 15	U67H0201R	0.8	16	8586
2001 Jan 15	U67H0301R	0.8	16	8586
2001 Jul 30	U6IZ0201R	0.8	17	9227
2002 Jan 17	U6IZ0301M	0.8	17	9227
2002 Aug 05	U8IP0201M	1.0	17	9332
2003 Feb 11	U8IP0301M	1.0	17	9332
2003 Aug 05	U8RM0201M	1.0	17	9887
2004 Jan 29	U8RM0301M	1.0	17	9887
2004 Aug 08	U9290201M	1.0	17	10112
2005 Jan 15	U9290301M	1.0	17	10112
2005 Aug 13	U9D30201M	1.0	17	10481
2006 Jan 30	U9D30301M	1.0	17	10481
2006 Sep 26	U9O50201M	1.0	17	10914
2007 Oct 17	UA0P0201M	1.0	17	11296
WFC3/UVIS Frames, F225W Filter				
2010 Jan 09	IB7J02010	1.0, 260	16	11786
2010 Dec 03	IBK702010	1.5, 265	16	12296
2011 Dec 05	IBTI02010	1.5, 265	16	12673
2012 Dec 02	IC1K02010	1.5, 236	16	13062
2013 Oct 25	ICA102010	1.5, 259	16	13468
2015 Jan 06	ICJX02010	1.5, 255	16	13876
WFC3/UVIS Frames, F953N Filter				
2016 Jul 11	ICVD02010	0.5, 2.5, 200	24	14342

Notes.

[a] Data set identifier for first observation made at each visit.

[b] Total number of individual frames obtained during each visit.

[c] HST proposal identification number. H.E.B. was PI for all of these programs.

[d] 0.11 s exposures were also taken in F467M and F547M on 1997 Jul 04 and 1998 Jan 02, in an attempt to determine the color of the companion; however, it was not detected in these frames.

Table 1 presents the HST observing log for μ Cas. For the WFPC2 imaging, knowing that the faint companion of μ Cas is cooler than the primary star, we selected the longest-wavelength filter available on the camera, which also had a narrow enough bandpass to permit a well-exposed but unsaturated image of the primary to be obtained in a short integration time. These considerations led to the choice of the F953N bandpass, a narrowband filter normally intended for imaging of the [S III] λ9530 nebular emission line. We placed μ Cas near the center of the Planetary Camera (PC) CCD detector, providing a plate scale of $\sim 0\farcs0456$ pixel^{-1}. For our initial two visits, we chose exposure times of 0.3 and 0.5 s, at four dither positions each. We made these exposures short enough to ensure that the primary's image would not be saturated, which indeed proved to be the case. The magnitude difference between A and B in this bandpass was measured to be 4.9 mag. Based on these frames, we increased the integration time to 1.0 s for the next three visits and obtained 15 dithered exposures per visit. These dithers used five different pointings, separated by several tenths of an arcsecond, and

---

[5] An earlier visual resolution was reported in a conference abstract by Wehinger & Wyckoff (1966), but the measurements (separation, position angle, and magnitude difference) are so discordant with subsequent findings that the detection appears to be spurious. According to Feibelman (1976), the claim was later withdrawn. Feibelman himself reported a partial resolution of the binary in photographs obtained in 1964 and 1965, but again his results are in poor agreement with the elements derived in subsequent work, including the present paper. Lippincott (1981) lists in her Table 4 other attempts to resolve the binary up to the early 1980s. With some prescience, she stated, "One observation by the Space Telescope in combination with ... the astrometric orbit should give the total mass of the system, as well as the individual masses." But Pierce & Lavery (1985) riposted that the suggestion of a single space-based observation being sufficient would "appear to be premature."

sampled five different pixel phases in both coordinates. Because images of the primary had a few saturated pixels in a few of these frames, we reduced the exposure time to 0.8 s for the next five visits and took 15–17 dithered exposures at each epoch. For the final 10 visits with the aging WFPC2 instrument, we increased the exposure time back to 1.0 s, obtaining 17 exposures per visit. For all exposures, we chose a telescope orientation such that the faint companion would lie away from the diffraction spikes and charge bleeding of the bright primary.

With the installation of the more sensitive WFC3 camera, we had no available combination of a long-wavelength filter and short exposure time that would reliably produce unsaturated images of μ Cas A. In order to obtain unsaturated WFC3 exposures, the best choice was the ultraviolet F225W bandpass —which meant that the dM companion would be extremely faint and require long exposures for detection. We therefore adopted a strategy that we also used for Procyon (see B15): at each dither position, we obtained a short unsaturated exposure of the primary and then, without moving the telescope, a long exposure to detect the companion. For the first WFC3 visit, we obtained eight dithered 1.0 s exposures combined with eight 260 s exposures at the same pointings. To reduce data volume and avoid interruptions for buffer dumps, we used a 512 × 512 subarray for all of our WFC3 exposures. The WFC3 UVIS channel has two CCD detectors (plate scale $0\rlap{.}''0396\ \mathrm{pixel}^{-1}$) with a small gap between them; for our first WFC3 visit we used UVIS1, but for the rest we used the better-characterized UVIS2. Based on results of the first WFC3 visit, we increased the short exposures to 1.5 s for the remainder of the F225W observations and adjusted the long-exposure integration times slightly so as to use all of the available target visibility time during the HST orbit.

The red companion star is very faint in the WFC3 F225W filter: we measured a difference of 9.9 mag relative to the primary. We continued to use this filter and observing strategy for five subsequent visits, but it became apparent that the astrometric precision was poorer than we had achieved in the far-red bandpass used with WFPC2. The situation was becoming worse as the orbital separation began to shrink rapidly and the companion was becoming embedded in the wings of the primary's image. Thus, for our final observation, we adopted an alternative approach, using the WFC3's version of the F953N filter. We obtained dithered exposures with integration times of 0.5 s (hoping for an unsaturated primary star—but not realized consistently), 2.5 s (for good unsaturated exposures of the companion), and 200 s (for an attempt to centroid saturated images of both stars using the diffraction spikes and features in the wings—see below).

To give an impression of the images obtained with the three different camera setups, we show false-color renditions of typical frames in Figure 1. The companion μ Cas B is marked with green circles. The top two images were taken with WFPC2/PC and the F953N filter in 1999 and 2007, showing the companion lying on an Airy ring of the primary in the first frame and well separated in the second. The bottom left frame was taken in 2012 with WFC3/UVIS in the ultraviolet F225W filter, in which the dM companion is relatively very faint. At the bottom right is a WFC3/UVIS F953N frame obtained in 2016.

3. HST Astrometric Analysis

For the astrometric measurements of separation and position angle (P.A.) for the μ Cas system, we have three sets of HST images. These are (1) WFPC2/PC frames in the F953N filter (1997–2007), (2) WFC3/UVIS frames in F225W (2010–2015), and (3) WFC3/UVIS frames in F953N (2016).

3.1. WFPC2 Images in F953N

In the WFPC2 F953N bandpass, we obtained a total of 312 individual frames over the 20 visits to μ Cas. We used a nominal gain of 15 electrons per data number and exposure times such that μ Cas A would just approach saturation. In only seven cases was there actually a saturated pixel at the center of A's image, and we discarded those frames from further analysis. In this long-wavelength bandpass there were well-detected images of the B companion (see Figure 1, top row).

For the astrometric centroiding, we used a technique of point-spread function (PSF) fitting. Our procedure was nearly identical to that described in detail by B15 for our analysis of unsaturated frames of Procyon, so we give only a brief description here. The primary difference was that the μ Cas frames were taken in a different filter than we used for Procyon (F218W).

To determine a highly oversampled PSF, we stacked the 305 frames using a preliminary set of centroid estimates for the A component. By fitting to this initial PSF, we updated the centroid positions of A. Then, the refined positions were used to create a new PSF. Iterating this procedure five times led to excellent convergence. Using this final PSF, in the form of a 5 × 5 array without the corners (i.e., 21 pixels), we determined each of the A-image centroid positions.

To centroid the companion's images in the same frames, we first had to remove light due to the wings and Airy rings of the primary star, which is particularly important at small angular separations (e.g., the top left frame in Figure 1). This was done by defining a large-scale PSF based on the images of A, extending out to the largest separation reached by B (suppressing pixels lying near B in each individual frame before combining all of the images). We then subtracted this PSF from the frames and then simply determined the positions of B by fitting the same PSF employed for A. As described in B15, the resulting x, y positions were corrected for the WFPC2 34th-row anomaly and for geometric distortion.

In order to convert the adjusted x, y positions to seconds of arc, we need the plate scale for WFPC2 F953N images. Unfortunately, this rarely used filter does not have a primary scale calibration. However, we found that the published plate scales for well-calibrated WFPC2 filters are strongly correlated with the index of refraction of MgF_2 at the effective wavelengths of the bandpasses. (This is due to the use of MgF_2 transmission optics in the camera.) Applying this relationship, we adopted a nominal plate scale of $0\rlap{.}''045575\ \mathrm{pixel}^{-1}$.

The scale for each image was then very slightly adjusted for differential velocity aberration, using the image-header keyword `VAFACTOR`. "Breathing" of the telescope tube induces small changes in focus, and thus changes in the PSF along with minor changes to the large-scale geometric distortion (see Gilliland 2005). These telescope responses tend to vary over the orbital visibility period. Since our observations at each epoch used a full visibility period, these effects will be somewhat averaged out. Remaining uncorrected residuals resulting from these effects are a likely source for the small remaining scatter in our astrometry, as discussed below (Section 7).

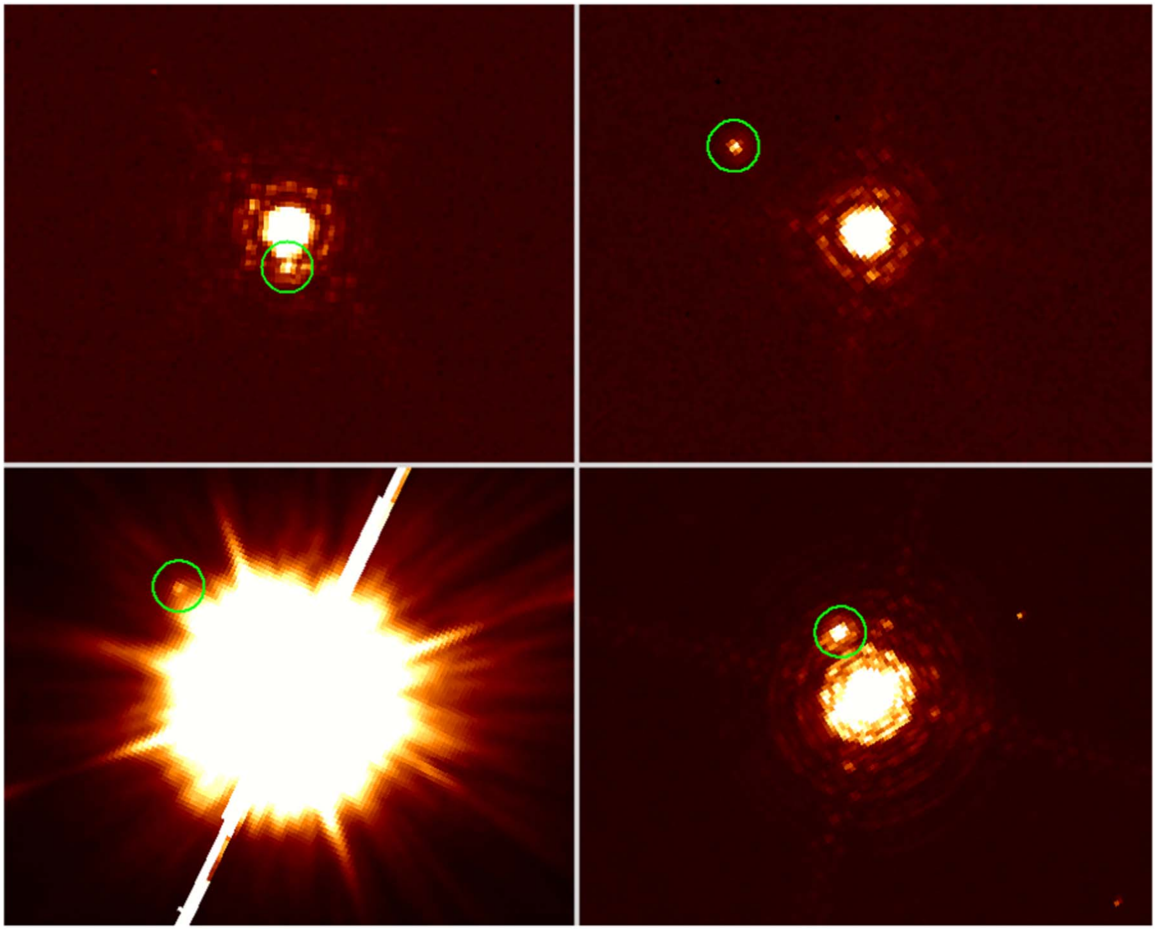

Figure 1. False-color renditions of HST images of μ Cas. Each frame is 4$''$0 high and has north at the top and east on the left. The companion star μ Cas B is marked with a green circle in each image. Top row: WFPC2/PC images in the F953N filter taken in 1999 (left) and 2007 (right); separations 0$''$349 and 1$''$389. Bottom row: WFC3/UVIS images in F225W (left) taken in 2012 and in F953N taken in 2016 (right); separations 1$''$333 and 0$''$607.

Finally, the orientation of each image on the sky was obtained from the `ORIENTAT` keyword in the image headers, which has an uncertainty of about ±0°03 (see B15). A small number of discordant measures were dropped (mostly due to cosmic-ray hits within the image of either star, or detector artifacts), and then the determinations at each epoch were combined into averages, with the uncertainties calculated from the standard errors of the means.

An issue emerged when we began to make orbital solutions for the binary using the WFPC2 astrometry. Over the last several years of WFPC2 data, there were increasingly large residuals, with alternating signs, for observations spaced about 6 months apart. Since the spacecraft roll angles differed by about 180° for successive visits, these offsets are plausibly attributable to the effect of charge transfer inefficiency (CTI) in the WFPC2 detectors. The amount of CTI increases with time, as the CCDs are exposed to the space environment. CTI leads to some of the charge in a stellar image falling behind as the image is read out, producing faint "tails" adjacent to the image, and thus slightly displacing its mean position in the detector y-direction. We derived an approximate empirical time-dependent correction for the CTI effect, as described in more detail in Appendix A, and applied it to all of the WFPC2 measurements. The final WFPC2 astrometric results are presented in the first 20 lines of Table 2.

3.2. WFC3 Images in F225W

In this series of observations, we obtained short and long exposures at each dithered telescope position. The image of A was unsaturated in the short exposures, and B was well detected in the long ones. We began by obtaining the drizzle-combined images ("drz" frames) from the standard HST pipeline.[6] Unlike the WFPC2 images, these frames have already been corrected for geometric distortion. They have cosmic rays removed, and the plate scale is given in the image headers. At each epoch, we have two pairs of short and long combined exposures.

We then proceeded similarly to the WFPC2 analysis described above. We determined an oversampled PSF by combining all of the μ Cas frames, as well as a selection of 22 F225W observations of other bright stars available in the archive. These had all been taken in the same subarray and UVIS2 chip as our μ Cas observations (except for our first WFC3 visit in UVIS1). Most of the archival frames are of white dwarfs that are much bluer than the components of μ Cas, but we saw no evidence of a color term in the PSF. As for the WFPC2 frames, the PSF determination converged after a few iterations. We then used PSF fitting to determine the final positions for component A.

---

[6] https://archive.stsci.edu/hst

Table 2
HST Astrometric Measurements of μ Cas B Relative to μ Cas A

UT Date	Besselian Date	Separation (arcsec)	J2000 Position Angle[a] (deg)
	WFPC2/PC Frames, F953N Filter[b]		
1997 Jul 04	1997.5057	0.4191 ± 0.0010	226.493 ± 0.092
1998 Jan 02	1998.0047	0.4454 ± 0.0009	214.181 ± 0.066
1998 Jul 22	1998.5544	0.4077 ± 0.0002	200.497 ± 0.075
1999 Feb 28	1999.1612	0.3490 ± 0.0004	179.581 ± 0.087
1999 Aug 04	1999.5906	0.3151 ± 0.0007	160.771 ± 0.101
2000 Feb 01	2000.0868	0.3221 ± 0.0006	137.050 ± 0.071
2000 Jul 15	2000.5390	0.3632 ± 0.0005	118.183 ± 0.064
2001 Jan 15	2001.0406	0.4313 ± 0.0004	102.617 ± 0.067
2001 Jul 30	2001.5773	0.5237 ± 0.0003	91.325 ± 0.057
2002 Jan 17	2002.0476	0.6103 ± 0.0004	84.393 ± 0.040
2002 Aug 05	2002.5934	0.7102 ± 0.0003	78.543 ± 0.059
2003 Feb 11	2003.1144	0.8028 ± 0.0003	74.109 ± 0.036
2003 Aug 05	2003.5942	0.8860 ± 0.0006	70.993 ± 0.036
2004 Jan 29	2004.0772	0.9637 ± 0.0002	68.262 ± 0.037
2004 Aug 08	2004.6039	1.0429 ± 0.0006	65.927 ± 0.040
2005 Jan 15	2005.0412	1.1071 ± 0.0003	64.020 ± 0.035
2005 Aug 13	2005.6175	1.1826 ± 0.0005	61.937 ± 0.035
2006 Jan 30	2006.0815	1.2368 ± 0.0003	60.405 ± 0.035
2006 Sep 26	2006.7400	1.3054 ± 0.0004	58.568 ± 0.034
2007 Oct 17	2007.7933	1.3931 ± 0.0003	55.798 ± 0.032
	WFC3/UVIS Frames, F225W Filter[c]		
2010 Jan 09	2010.0236	1.4795 ± 0.0037	50.711 ± 0.072
2010 Dec 03	2010.9222	1.4625 ± 0.0058	48.697 ± 0.284
2011 Dec 05	2011.9264	1.4166 ± 0.0018	46.204 ± 0.076
2012 Dec 02	2012.9204	1.3326 ± 0.0011	43.439 ± 0.099
2013 Oct 25	2013.8179	1.2365 ± 0.0008	40.960 ± 0.123
2015 Jan 06	2015.0150	0.9969 ± 0.0007	37.122 ± 0.082
	WFC3/UVIS Frames, F953N Filter		
2016 Jul 11	2016.5261	0.6069 ± 0.0028	25.450 ± 0.280

Notes.

[a] Note that the P.A.s are referred to the equator of J2000, not to the equator of observation epoch as is the usual practice for ground-based visual-binary measurements.

[b] Corrected for charge transfer inefficiency, as described in Section 3.1 and Appendix A.

[c] Corrected for chromatic aberration, as described in Section 3.2 and Appendix B.

In the long-exposure frames, the faint B companion is embedded in the bright wings of A (see Figure 1, bottom left panel). We determined a large-scale PSF from the observations of A and subtracted it from the images before measuring the position of B, using the same oversampled PSF determined above.

Our first WFC3 observations, taken in early 2010, present a special problem: they used the UVIS1 chip, for which there are insufficient observations useful for determining an oversampled PSF. We therefore used the UVIS2 PSF for the astrometry of these frames.

When we carried out our initial orbital fits to the HST data, the WFC3+F225W measurements stood out as having unusually large residuals (up to about 40 mas), compared to those from the earlier WFPC2 series and the final WFC3 observation described below. Upon investigation, we eventually realized that this problem arises because of a small amount of chromatic aberration in the WFC3 camera, combined with the fact that the F225W filter has a significant red leak. The result is that most of the light detected from the very red μ Cas B is actually transmitted through the red leak, rather than the main bandpass of the UV filter, which transmits most of the light of the primary star. Thus, the image of μ Cas B is slightly displaced relative to that of the bluer A component. We were able to derive an approximate correction for this effect, as discussed in detail in Appendix B.

As with WFPC2, as discussed in the previous subsection and in Appendix A, WFC3 has shown a progressive increase of CTI with time, potentially contributing errors to our position measurement of the very faint μ Cas B relative to the much brighter A. Our astrometric analyses were performed using the "drz" image products provided by the STScI pipeline; the "drc" products that additionally have been corrected at the pixel level for CTI were not available at the time of our analyses. We have subsequently compared the drc and drz images, and they do not show discernible shifts of the position of B in our data. We also performed an empirical search for CTI-induced position shifts, as we did for WFPC2, but did not find a significant correlation of the x, y residuals relative to a preliminary orbit fit as a function of time. In the WFC3 F225W images, the B component is well within an extended halo of light from the much brighter A, producing a local sky background of several hundred electrons per pixel at its position. This background likely suppresses any significant CTI losses. Thus, we did not make any corrections for CTI in the drz images.

The next six lines in Table 2 contain the results of these measurements, adjusted for differential chromatic aberration as described above. The uncertainties were calculated based on the internal scatter of the pairs of measurements at each epoch, combined in quadrature with an estimated error of $0\overset{\prime\prime}{.}0007$ from telescope pointing drift between the short and long exposures (see B15 for details), and the uncertainty in telescope orientation described above. We have not attempted to include the additional systematic uncertainties due to the approximate nature of the aberration correction. Because of this, we will give the F225W measurements a lower weight than the other determinations when we calculate an orbital fit below.

3.3. WFC3 Images in F953N

Our final 2016 observations of μ Cas were made with the WFC3's long-wavelength F953N filter. We obtained dithered images with short (0.5 s), medium (2.5 s), and long (200 s) exposures. The short exposures proved to be a mixture of saturated and unsaturated images of A and were discarded. In the medium-exposure frames, A is saturated, and in the long-exposure images both stars are saturated. With the F953N exposures, we have the advantage that the same filter was used for our studies of Procyon (B15) and Sirius (B17). Thus, we can use very similar reduction techniques. As those papers describe, we employed two different methods for centroiding the stellar images. One used PSF fitting, based on selected regions in the PSF in the unsaturated outskirts. The other used the diffraction spikes in the overexposed images, taking their inferred intersection point as the centroid. As noted in B15 and B17, the two methods give results that agree well. In the final line in Table 2 we give the average separation and P.A. obtained from the two methods.

As with the WFC3 observations in F225W, the well-exposed image of B in the F953N frames sits on top of hundreds of electrons from the nearby A. Fitting the location of B in the drc images shows no difference from those we derived using drz frames. The high sky background, coupled with well-exposed

Table 3
Ground-based Astrometric Measurements of μ Cas B Relative to μ Cas A

Besselian Date	Separation (arcsec)	Position Angle (deg)	References[a]
1973.787	0.35 ± 0.04	24 ± 3	(1)
1974.650	0.23 ± 0.01	333.9 ± 2	(2)
1983.20	0.98 ± 0.024	55.8 ± 0.7	(3)
1983.494	0.93 ± 0.06	224.3 ± 2.6	(4)
1983.7072	1.074 ± 0.042	61.9 ± 3.0	(5)
1984.126	1.118 ± 0.023	63 ± 2	(6)
1984.9132	1.251 ± 0.030	59.3 ± 1.3	(5)
1985.0842	1.320 ± 0.027	60.6 ± 1.1	(5)
1985.8448	1.425 ± 0.016	59.47 ± 0.51	(5)
1990.6836	1.36 ± 0.076	48.2 ± 3.1	(7)
1991.7268	1.41 ± 0.051	48.6 ± 6.8	(7)
1994.6563	0.73 ± 0.02	28.5 ± 0.7	(8)
1994.8069	0.66 ± 0.02	27.0 ± 0.8	(8)
2003.5663	0.86	70.2	(9)
2004.6632	1.042 ± 0.020	65.0 ± 1.3	(10)
2014.7581	1.0707 ± 0.0036	38.3 ± 0.51	(11)
2014.7581	1.0727 ± 0.0036	38.1 ± 0.51	(11)
2015.5448	0.9018 ± 0.0043	34.5 ± 1.0	(12)
2015.5448	0.8991 ± 0.0043	32.0 ± 1.0	(12)
2016.0337	0.7560 ± 0.0037	30.9 ± 1.0	(12)
2016.0337	0.7510 ± 0.0037	31.0 ± 1.0	(12)
2016.0474	0.7513 ± 0.0037	30.6 ± 1.0	(12)
2016.0474	0.7589 ± 0.0037	27.7 ± 1.0	(12)

Note.
[a] References: (1) Wickes & Dicke 1974; (2) Wickes 1975; (3) McCarthy 1984; (4) Pierce & Lavery 1985; (5) Haywood et al. 1992; (6) Karovska et al. 1986; (7) McCarthy et al. 1993; (8) Drummond et al. 1995; (9) L. Roberts, Palomar AO system, private communication; (10) Christou & Drummond 2006; (11 and 12) Horch et al. (2015, 2019); observations at each epoch were made in two different bandpasses.

B images for the F953N exposures, likely suppressed any significant CTI losses.

4. Ground-based Measurements and Parallax

4.1. Astrometry of μ Cas B

Although the available ground-based astrometric measurements of μ Cas B relative to A generally do not have the precision of the HST data, they cover more than twice the time interval. Thus, they are useful for constraining orbital parameters, especially the orbital period. Table 3 lists the published ground-based astrometric observations of μ Cas B of which we are aware, along with one unpublished measurement from a private communication.

4.2. Parallax

μ Cas is not included in the recent Gaia Data Release 2 (DR2; Gaia Collaboration et al. 2018), likely because of the star's brightness and large proper motion. However, parallax measurements are available from several earlier studies. Lippincott & Wyckoff (1964) list their own measurement, along with three earlier determinations, but since all of their stated uncertainties are relatively large compared to more recent values, we did not utilize them in our study.

The five parallax determinations that we considered are listed in the first five lines in Table 4: (1) Lippincott (1981) obtained the parallax from measurements of photographic plates taken at the Sproul Observatory on 215 nights between 1937 and 1980, converted from relative to absolute using a statistical mean parallax for the reference stars. Since precise parallaxes are now available for each of the background stars from Gaia DR2, we calculated the mean of these and made a (small) adjustment to her result. She had assumed a mean parallax of 0.″0041, but the DR2 mean is 0.″0019. (2) Russell & Gatewood (1984) measured the parallax using 371 plates from the Allegheny Observatory taken between 1933 and 1978. We again made a small adjustment to their result, based on the mean Gaia parallaxes for their reference stars of 0.″0025 versus their assumed 0.″0030. (3) Harrington et al. (1993) measured 68 plates obtained at the U.S. Naval Observatory between 1984 and 1990 and similarly adjusted from relative to absolute using a statistical algorithm. Here the adjustment based on the mean Gaia reference-star parallaxes is very small, 0.″0017 as compared to their 0.″0015. (4) Heintz (1994) presented the final Sproul photographic results, from 251 observations over 55 yr. He did not give details of the reference stars, so we assumed that they were the same as used by Lippincott, and we applied the same DR2-based correction to absolute. (5) The absolute parallax was measured by the Hipparcos mission (van Leeuwen 2007).

Table 4
Parallax of μ Cas

Source	Parallax (arcsec)	References
Sproul	0.1318 ± 0.0011[a]	Lippincott (1981)
Allegheny	0.1363 ± 0.0033[a]	Russell & Gatewood (1984)
USNO	0.1326 ± 0.0023[a]	Harrington et al. (1993)
Sproul	0.1329 ± 0.0017[a]	Heintz (1994)
Hipparcos	0.13238 ± 0.00082	van Leeuwen (2007)
Weighted mean	0.13266 ± 0.00069	Adopted[b]

Notes.
[a] Adjusted for mean Gaia DR2 parallax of reference stars; see text.
[b] Lippincott (1981) value not included in the mean; see text.

The five results are in good agreement. Omitting the earlier Sproul measurement as being superseded by the later one, we adopt the weighted mean of the remaining four measurements (which is very close to the Hipparcos value), as given in the final line of Table 4.

4.3. Photocenter Motion of μ Cas A

To obtain the individual masses of the two components, we require the semimajor axis of the absolute orbital motion of μ Cas A. Because of the large magnitude difference between the components, we take the photocenter of the system to represent this motion. Measurements of the photocenter motion were made in the parallax studies of Lippincott (1981) and Russell & Gatewood (1984). Lippincott listed normal points for her measurements of the photocentric orbit (her Table 2). Russell & Gatewood (1984) did not tabulate their individual measurements, but J. Russell had provided them privately to Drummond et al. (1995). Through the kindness of J. Russell and J. Drummond, these measurements were communicated to us. Because they have not been published previously, we list them in Table 5. These data will be included as input to the final orbital solution described below.

Table 5
Photocenter Motion for μ Cas A Measured by Russell & Gatewood (1984)[a]

Epoch	Offset (arcsec)	Position Angle (deg)
1933.0160	0.1471	38.1238
1933.7960	0.0655	10.6570
1934.6460	0.0664	309.5121
1935.6290	0.0751	284.2946
1937.6650	0.1494	257.3742
1938.9510	0.1500	272.5285
1939.6970	0.2092	243.6260
1940.6360	0.2395	248.4918
1942.9270	0.2827	231.6788
1943.8620	0.2651	235.2058
1944.6930	0.2654	231.6809
1945.7420	0.2694	230.8118
1946.7660	0.2662	232.2710
1947.8000	0.2540	226.8881
1948.7960	0.2193	225.9624
1949.8390	0.1795	224.9168
1950.8150	0.1475	213.4607
1951.7580	0.1158	213.0443
1952.7880	0.0615	142.6767
1953.7200	0.0684	50.9950
1954.7770	0.0903	25.8460
1955.6750	0.0739	8.4718
1957.8580	0.0832	293.9446
1964.8380	0.2305	236.1935
1965.7650	0.2628	240.7150
1966.9150	0.2556	239.1292
1968.6880	0.2713	229.5558
1969.7280	0.2589	228.6600
1971.9450	0.1330	218.8055
1972.6250	0.1959	226.5597
1975.8830	0.0829	33.0381
1976.7680	0.0772	43.5241
1977.6930	0.0437	5.3173
1978.8030	0.0366	359.9587

Note.
[a] Previously unpublished data, kindly communicated by J. Drummond and J. Russell.

4.4. Radial Velocities

RV measurements potentially provide useful constraints on the orbital solution, especially since they cover more than a century. They also resolve the ambiguity as to the orientation of the orbit (i.e., which star is in front). We compiled the RV data published in the following papers: (1) Worek & Beardsley (1977): 100 photographic measurements, 1900–1976. (2) Abt et al. (1980): three photographic measurements, 1967–1975. (3) Beavers & Eitter (1986): 22 RV spectrometer measurements, 1976–1983. (4) Abt & Willmarth (1987): 12 CCD measurements, 1984–1985. (5) Abt & Willmarth (2006): 24 CCD measurements, 2000–2003. (6) Agati et al. (2015): 45 CORAVEL measurements, 1977–1999, including a re-reduction of data published earlier by Jasniewicz & Mayor (1988) and Duquennoy et al. (1991).

5. Elements of the Relative Visual Orbit of μ Cas B

5.1. Orbital Solution

Our determination of the orbital elements largely follows the procedures described in detail for Procyon and Sirius by B15 and B17. We describe the main points of the fitting method below.

The first step was to adjust all of the measurements, HST and ground-based, to the J2000 standard equator and epoch. We used the formulations given by van den Bos (1964) in order to correct for (1) precession (except for the HST measures, which are already in the J2000 frame), (2) the change in direction to north due to proper motion, (3) the changing viewing angle of the three-dimensional orbit due to proper motion, and (4) the steadily decreasing distance of the system due to RV. All of these corrections are small relative to the observational uncertainties for the ground-based data, and they are also small for the HST data because their epochs are all so close to 2000.0.

We determined elements for the relative visual orbit and photocenter motion via an eight-parameter fit to the combined set of J2000-corrected HST and ground-based measurements of the B–A separation and P.A. (Tables 2 and 3, with adjustments applied) and of the photocenter motion of A (Lippincott 1981, and our Table 5). This fit employed a Newton–Raphson method to minimize the χ^2 between the measured and fitted positions, by calculating a first-order Taylor expansion for the equations of orbital motion. The procedure results in a solution for the period P, time of periastron passage T_0, eccentricity e, semimajor axis a, inclination i, P.A. of the line of nodes Ω, argument of periastron ω_B as referenced to μ Cas B, and the semimajor axis of the photocenter motion a_A.

Before computing the joint fit to all data, we fit an orbit to each set of measurements independently and scaled the uncertainties in order to force the reduced χ^2_ν to unity. We scaled the error estimates for WFPC2 by a factor of 2.7, WFC3 by 7.3, and the ground-based measurements by 1.8, compared with the values listed in Tables 2 and 3. For the ground-based observations we deleted the 1983.20 measurement, because it was $\sim 4\sigma$ discrepant from the initial orbit fit. The large uncertainty scale factor found for the WFC3 data is perhaps not surprising, given the approximate nature of the chromatic aberration corrections described in Appendix B. The smaller scaling for WFPC2 probably reflects remaining systematic errors due to telescope breathing and CTI, as discussed in Section 3.1. For the photocenter motion, we assumed equal uncertainties in separation of $0\farcs0175$ for all of the measurements and scaled the uncertainties in P.A. to produce equal uncertainties in R.A. and decl.. The final orbital parameters determined from the joint fit to the visual orbit and photocenter motion are given in Table 6.

Figure 2 depicts the orbit of μ Cas B. The top panel plots the positions of B relative to A as measured by HST, and the bottom panel shows the ground-based measurements. In both panels the black ellipse shows our orbital fit. In the top panel the filled black circles mark the HST measurements from Table 2, with the small adjustments described above applied. The open blue circles are the predicted positions from our orbital parameters. The fit agrees well with the WFPC2 data (1997–2007) at the scale of the figure, as does the final WFC3 observation in 2016. For the WFC3 F225W observations, 2010–2015, there are evident small departures from the fit, likely arising from uncertainties in the correction for chromatic aberration, as just noted above.

The bottom panel of Figure 2 plots the ground-based measurements from Table 3, again with the small adjustments applied. The blue filled circles mark the observations from

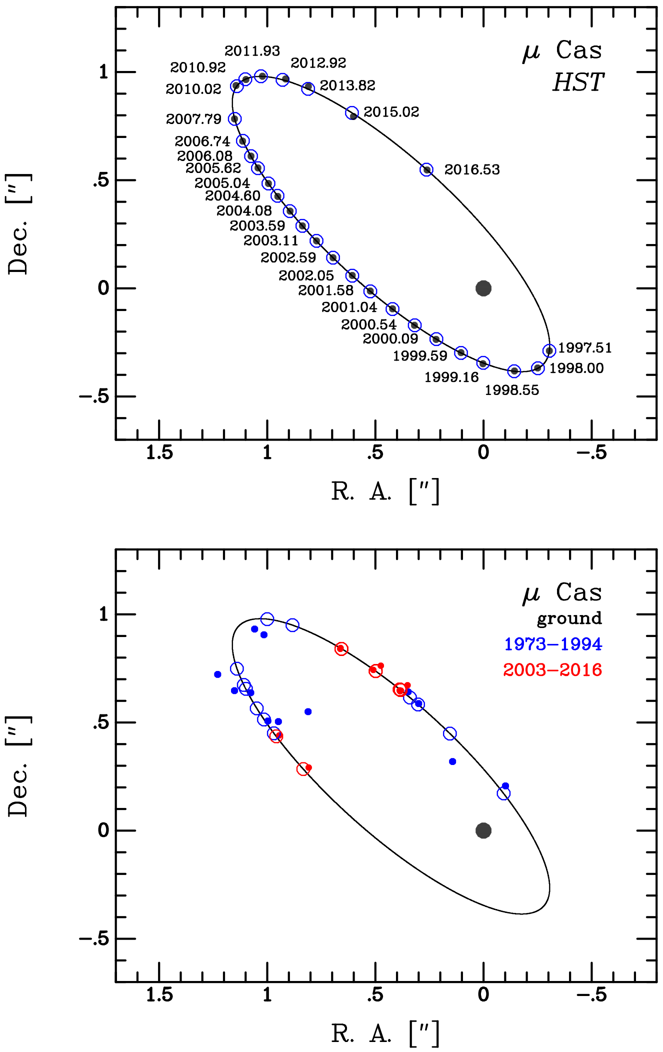

Figure 2. Top panel: HST observations of the orbit of μ Cas B relative to A (which is plotted as a large black circle at the origin). Filled black circles show the HST measurements (listed in Table 2), each one labeled with the date of observation. The black ellipse plots our orbital fit from Section 5.1. Open blue circles mark the predicted positions from the orbital fit. Bottom panel: ground-based measurements (listed in Table 3). The black ellipse is our orbital fit from the top panel. Blue filled circles plot the observations from 1973 to 1994, and red filled circles show the measurements from 2003 to 2016. The open blue and red circles mark the corresponding predicted positions based on our orbital fit.

Table 6
Elements of μ Cas Visual Orbit (J2000)

Element	Value
Orbital period, P (yr)	21.568 ± 0.015
Semimajor axis, a (arcsec)	0.9985 ± 0.0013
Inclination, i (deg)	110.671 ± 0.064
Position angle of node, Ω (deg)	223.868 ± 0.064
Date of periastron passage, T_0 (yr)	1997.2235 ± 0.0067
Eccentricity, e	0.5885 ± 0.0011
Longitude of periastron, ω_B (deg)	330.37 ± 0.18
Photocenter semimajor axis, a_A (arcsec)	0.1882 ± 0.0023

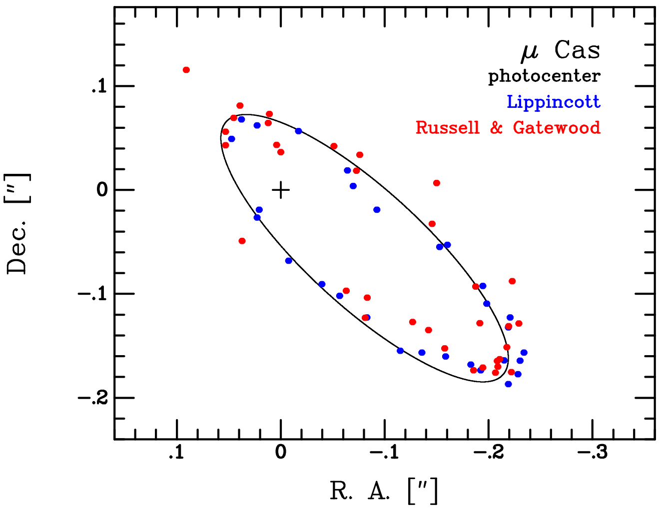

Figure 3. Offsets of the μ Cas photocenter relative to the center of mass (plus sign), from the ground-based measurements of Lippincott (1981) (filled blue circles) and Russell & Gatewood (1984) (from our Table 5; filled red circles). The black ellipse shows the fit from our joint orbital solution.

1973 through 1994, and the red filled circles those from 2003 to 2016. The open circles, with the same color-coding, show the corresponding ephemeris positions from our orbit solution. As can be seen, the early observations had significant errors. The twenty-first-century observations have noticeably smaller errors.

5.2. Photocenter Orbit

Figure 3 plots the positions of the photocenter of μ Cas relative to the center of mass. The filled blue and red circles are the Sproul and Allegheny measurements of Lippincott (1981) and of Russell & Gatewood (1984) (from our Table 5), respectively. The black ellipse is our orbital fit from our χ^2 solution, with a semimajor axis of $a_A = 0.''1882 \pm 0.''0023$. Lippincott obtained a value of $0.''1862 \pm 0.''0013$ from her data, and Russell & Gatewood found $0.''1900 \pm 0.''0038$ from theirs. Drummond et al. (1995) carried out a joint solution from their own astrometry and combining both the Lippincott and Russell & Gatewood photocenter motions, obtaining $a_A = 0.''1908 \pm 0.''0043$. All of these earlier results are in reasonable agreement with our final value.

5.3. Radial Velocity Curve

We attempted to add the μ Cas A RV semiamplitude, K_A, and the center-of-mass RV, γ, as ninth and 10th parameters in a joint orbital fit. We first tried to use all of the RV measurements from the references quoted in Section 4.4. However, it was apparent that the earlier, mostly photographic, RV data have significantly larger errors than the later values obtained with digital detectors, and that there are systematic offsets between different observatories. We then considered only the modern RV measurements of Abt & Willmarth (2006) and Agati et al. (2015) (as was done by Agati et al. in their discussion of μ Cas). This 10-parameter fit produced larger parameter uncertainties than the purely astrometric eight-parameter solution described above (Table 6). Moreover, this solution resulted in an RV semiamplitude of $K_A = 2.43 \pm 0.09\ \mathrm{km\ s^{-1}}$. A value this large, when combined with the measured photocenter semimajor axis, a_A, implies a distance to the system about 22% larger than given by the directly measured parallax. For these reasons, we will retain the orbital elements from the purely astrometric solution (Table 6) in the discussion below.

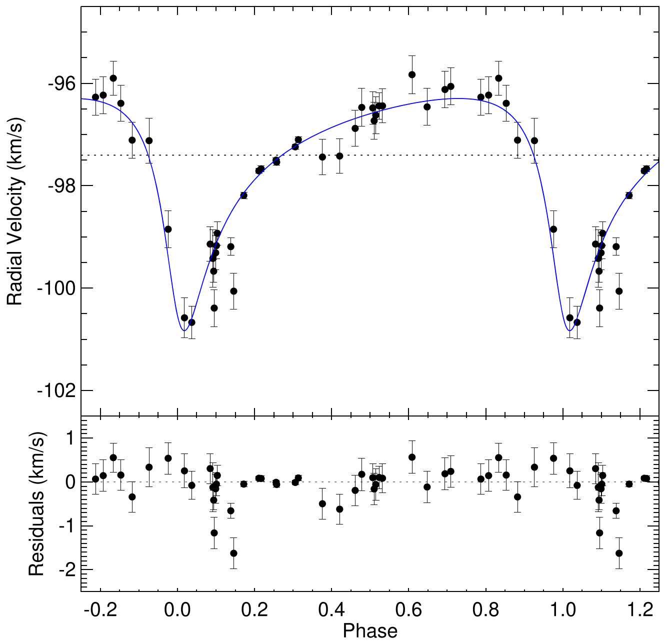

Figure 4. Top panel: RVs for μ Cas A (filled black circles) vs. orbital phase. Measurements are from Abt & Willmarth (2006) and Agati et al. (2015). Velocities obtained within 7 days of each other have been combined into normal points. The blue line shows the velocity curve predicted based on the adopted parallax and our eight-parameter fit to the astrometry. Bottom panel: residuals from the predicted velocities.

The RV measurements nevertheless provide a useful check on our orbital solution. In the top panel of Figure 4 we plot the Abt & Willmarth (2006) and Agati et al. (2015) RV measurements versus orbital phase.[7] In this plot, measurements obtained within 7 days of each other have been combined into normal points using weighted means. Based on the astrometric parameters and parallax, we predict an RV semiamplitude of $K_A = 2.27 \pm 0.03\ \mathrm{km\ s^{-1}}$. The blue line in the top panel shows the RV curve predicted by our orbital elements, where we have solved only for the center-of-mass RV, obtaining $\gamma = -97.40 \pm 0.03\ \mathrm{km\ s^{-1}}$. The bottom panel plots the residuals of the observations versus the predicted values. The predictions appear to agree well with the measurements, especially the values with small uncertainties from Abt & Willmarth (2006). The larger K_A that we found in the 10-parameter fit arose primarily from a few slightly discordant CORAVEL values around orbital phases 0.09–0.14; this K_A differs by only $\sim 1.8\sigma$ from the astrometrically predicted value.

6. Dynamical Masses

6.1. Masses of μ Cas A and B

To calculate the dynamical masses of μ Cas A and B, we employed the usual formula for the total system mass, $M = M_A + M_B = a^3/(\pi^3 P^2)$. The individual masses are then obtained using $M_A = M(1 - a_A/a)$ and $M_B = M\, a_A/a$. In these equations the masses are in $M_\odot$, a and π are the semimajor axis and parallax in arcseconds, respectively, and P is in years.

Table 7 presents the dynamical masses given by Drummond et al. (1995), Lebreton et al. (1999), and Horch et al. (2019) in Columns (2), (3), and (4), respectively. (The Lebreton et al. 1999 value was simply the Drummond et al. 1995 result adjusted to the Hipparcos parallax.) Our results are in the final column. They are in good agreement with the previous determinations, but the uncertainties are significantly smaller.

6.2. Error Budget

Table 8 shows the contributions of the uncertainties of each orbital parameter to the overall uncertainties of the dynamical masses of μ Cas A and B. The uncertainty in the mass of A is almost entirely due to the error in the adopted parallax. For the mass of B, the uncertainty is due about equally to the uncertainties in the parallax and those in the semimajor axis of the photocenter orbit, a_A. A more precise parallax from Gaia DR3 would provide a significant reduction in the uncertainties of the dynamical masses.

7. Astrometric Residuals and Limits on Third Bodies

In Figure 5 we plot the residuals between the HST astrometric measurements and our final orbital solution (Section 5.1 and Table 6) versus observation date. The top panel shows the residuals in R.A., and the bottom panel plots them in decl. Black points represent the residuals for the WFPC2+F953N observations, blue shows them for WFC3+F225W, and red plots them for the single WFC3+F953N measurement. The WFC3 data have relatively large error bars and a few very large residuals; these are plausibly due to uncertainties in the correction for chromatic aberration for the F225W data and also to the large magnitude difference in the WFC3 observations, an increasingly important source of error as the binary separation decreased. The residuals for the WFPC2+F953N combination are much smaller but still have some outliers that exceed the formal uncertainties. These likely arise from telescope breathing and CTI, as discussed above.

Figure 5 indicates that there is no convincing evidence for periodic perturbations with semiamplitudes of more than ∼2–3 mas, based on the WFPC2+F953N astrometry. The long-term stability of third bodies orbiting around individual stars in a binary system has been studied numerically by, among others, Holman & Wiegert (1999). Using the results in their Table 1 and the parameters of the present-day μ Cas binary, we find that the longest periods for stable third-body orbits in the system are about 1.07 yr for a body orbiting μ Cas A and 0.74 yr for one orbiting μ Cas B.

We calculated the semimajor axes of the astrometric perturbations of both stars that would result from being orbited by substellar companions of masses ranging from 5 to 60 M_{Jup} (where M_{Jup} is the mass of Jupiter, 0.000955 $M_\odot$) and for orbital periods up to the stability limits given above. The results are plotted in Figure 6. For a semiamplitude limit of 3 mas, the figure indicates that companions of μ Cas A or B of $\sim 20\, M_{\mathrm{Jup}}$ or less or $\sim 8\, M_{\mathrm{Jup}}$ or less, respectively, could escape astrometric detection at periods close to the stability limit. At shorter periods, successively higher masses could go undetected by astrometry. High-precision RV studies of μ Cas A could set tighter limits on third bodies orbiting the primary star at short periods.

8. Astrophysical Parameters of μ Cas A

As a well-known bright, moderately metal-poor, high-velocity star, μ Cas A has been the subject of numerous observational investigations. It is included among three dozen

---

[7] Abt & Willmarth (2006) did not list uncertainties for their individual measurements; based on the discussion in their text, we adopted $\pm 0.10\ \mathrm{km\ s^{-1}}$ for each velocity.

Table 7
Dynamical Masses for the μ Cas System

Quantity	Drummond et al. (1995)	Lebreton et al. (1999)	Horch et al. (2019)	This Paper
Total mass, $M_A + M_B$	$0.915 \pm 0.060\ M_\odot$	⋯	$0.906 \pm 0.023\ M_\odot$	$0.9168 \pm 0.0148\ M_\odot$
Mass of μ Cas A, M_A	$0.742 \pm 0.059\ M_\odot$	$0.757 \pm 0.060\ M_\odot$	⋯	$0.7440 \pm 0.0122\ M_\odot$
Mass of μ Cas B, M_B	$0.173 \pm 0.011\ M_\odot$	⋯	⋯	$0.1728 \pm 0.0035\ M_\odot$

Table 8
Error Budgets for μ Cas System Dynamical Masses

Quantity	Value	Uncertainty	$\sigma(M_A)$ ($M_\odot$)	$\sigma(M_B)$ ($M_\odot$)
Absolute parallax, π	0.13266	±0.00069 arcsec	0.0116	0.0027
Semimajor axis, a	0.9985	±0.0013 arcsec	0.0031	0.0004
Semimajor axis for A, a_A	0.1882	±0.0023 arcsec	0.0021	0.0021
Period, P	21.568	±0.015 yr	0.0010	0.0002
Combined mass uncertainty			0.0122	0.0035

well-studied “Gaia FGK benchmark stars” (e.g., Jofré et al. 2014; Heiter et al. 2015; Jofré et al. 2018, and references therein). Observational data on μ Cas A were reviewed extensively 5 yr ago by Bach (2015). We discuss and update the astrophysical parameters of the star in this section.

8.1. Angular Diameter

The angular diameter of μ Cas A was measured with the CHARA Array interferometer and reported by Boyajian et al. (2008, hereafter B08). They obtained a physical diameter (corrected for limb darkening) of 0.973 ± 0.009 mas. At the distance of μ Cas (Table 4), this corresponds to a physical radius of $0.789 \pm 0.008\ R_\odot$. When the distance and absolute luminosity of a star are known, measurement of the angular diameter allows its effective temperature, $T_{\rm eff}$, to be calculated from first principles. This can be compared with $T_{\rm eff}$ values inferred from spectroscopic and/or photometric data.

A few recent authors have noted discrepancies between effective temperatures of stars determined from spectroscopic and photometric measurements and those obtained from interferometric diameters (e.g., Casagrande et al. 2014; Karovicova et al. 2018; White et al. 2018). These discordances typically arise for stars with angular diameters close to the interferometric resolution limit ($\lesssim$1 mas) in the near-infrared K band, in the sense that the measured sizes often appear systematically larger than expected from the spectroscopic or photometric effective temperatures. To investigate whether the B08 diameter measurement of μ Cas A could have been impacted by these possible systematics, we re-reduced the archival B08 data by passing them through the most recent version of the reduction pipeline for CHARA Classic data.[8]

The latest code differs in the method used to compute the visibilities (integrating the power spectrum, vs. fringe-fitting functions) and the computation of the noise. Our new reduction yields a diameter 8% smaller, and thus an effective temperature 4% larger, than the values derived by B08. The difference between the old and new results suggests that there could be a problem with the interferometric diameter of μ Cas A published by B08. However, a full evaluation of this apparent discrepancy is beyond the scope of the present paper. The B08 measurement was made in the K band in the near-infrared. We note that a measurement of the angular diameter of μ Cas A using higher spatial resolution observations in the near-infrared H band, or at visible wavelengths, could provide a tighter constraint. In the meantime, in the following discussion we will retain the B08 diameter measurement.

8.2. Chemical Composition

For the Gaia benchmark stars, there is detailed information available on their chemical compositions, assembled from extensive high-resolution spectroscopic studies. Jofré et al. (2018) tabulate abundances of 20 individual metals in μ Cas A. Further details are given by Casamiquela et al. (2020). The carbon and oxygen contents of the star have been determined by Luck & Heiter (2005) and Luck (2017).

8.3. Stellar Parameters

In Table 9 we list physical parameters of μ Cas A and the literature sources from which they are quoted. Row 1 gives the dynamical mass determined in this paper. The radius and absolute luminosity in rows 2 and 3 of the table are corrected slightly from the cited literature values by adopting the parallax we give in Table 4.

Since we have directly measured the mass of μ Cas A and its radius and luminosity are known, we can calculate its effective temperature and surface gravity from first principles. These are listed in rows 4 and 5 of the table. We find $T_{\rm eff} = 5306 \pm 31$ K. A compilation of the parameters $T_{\rm eff}$ and $\log g$ for μ Cas A from published spectroscopic and photometric analyses is given by Heiter et al. (2015). For the effective temperature, they find a mean of $T_{\rm eff} = 5341$ K, with an appreciable standard deviation of 92 K, from seven determinations based on spectroscopy, and 5338 K with $\sigma = 82$ K from four photometric determinations. These values are slightly ($\sim 1\sigma$) higher than the $T_{\rm eff}$ that we calculate directly from the radius and luminosity. An even higher effective temperature of 5403 K[9] was found by Casagrande et al. (2010), based on the infrared flux method (IRFM). The more recent PASTEL literature compilation (Soubiran et al. 2016, version of 2020 January 30)[10] lists some 39 determinations of the atmospheric

---

[8] http://www.chara.gsu.edu/tutorials/classic-data-reduction

[9] An uncertainty was not given explicitly, but it is probably about ±50 K, judging from their findings for the majority of the stars in their sample.

[10] https://vizier.u-strasbg.fr/viz-bin/VizieR?-source=B/pastel

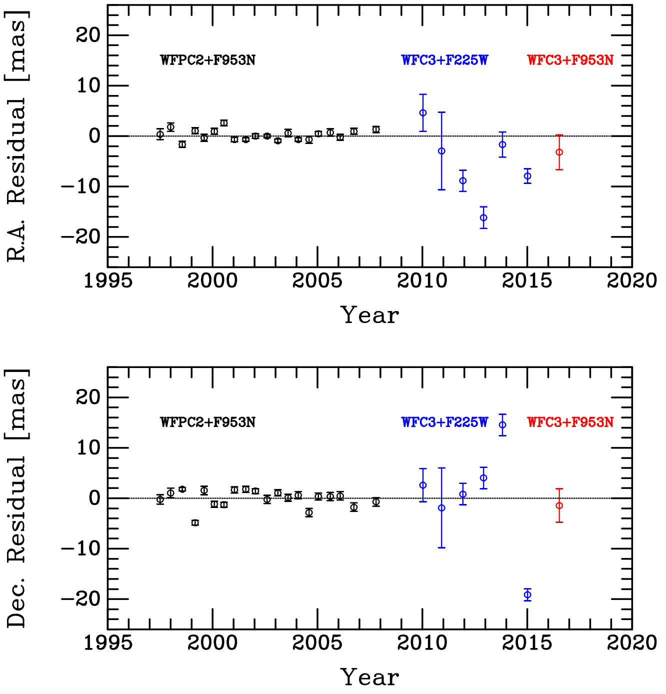

Figure 5. Residuals (in the sense observed minus ephemeris) for the HST astrometry, in R.A. (top panel) and decl. (bottom panel). Color-coding indicates the three different camera-plus-filter combinations that were used.

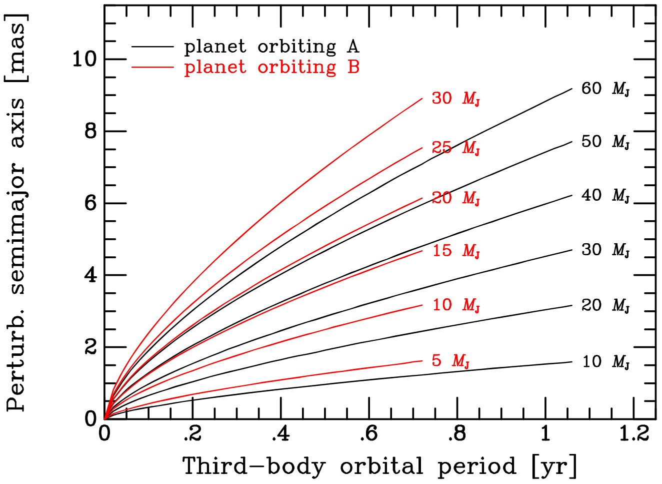

Figure 6. Astrometric perturbations that would result from planetary or brown dwarf companions of μ Cas A (black curves) or μ Cas B (red curves), with the masses of the perturbers (in units of the Jovian mass) indicated in the labels. Calculations were made for periods up to the orbital-stability limits of bodies with orbital periods of $\sim$1.07 yr (companions of μ Cas A) or $\sim$0.74 yr (companions of μ Cas B). The y-axis is the semimajor axis of the resulting astrometric perturbation of A or B in milliarcseconds.

parameters of μ Cas A (although some are republications of the same values). Among the 26 published in the twenty-first century, the effective temperatures range from 5240 to 5720 K. We return to the subject of the effective temperature in the next section.

For the surface gravity, eight determinations from spectroscopic analyses, summarized by Heiter et al. (2015), gave a mean of $\log g = 4.51$ with $\sigma = 0.20$. Here the agreement with our value of 4.515 ± 0.011, calculated from the radius and the dynamical mass, is excellent.

Table 9
Physical Properties of μ Cas A

Parameter	Value	Source[a]
Mass, M	$0.7440 \pm 0.0122\ M_\odot$	(1)
Radius, R	$0.789 \pm 0.008\ R_\odot$	(2)
Luminosity, L	$0.445 \pm 0.005\ L_\odot$	(3)
Effective temperature, $T_{\rm eff}$	5306 ± 31 K	(4)
Surface gravity, $\log g$ (cgs)	4.515 ± 0.011	(5)
Surface iron abundance, [Fe/H]	-0.81 ± 0.03	(6)
α-element abundance, $[\alpha/Fe]$	$+0.3$	(7)
Carbon abundance, [C/Fe]	$+0.08 \pm 0.08$	(8)
Oxygen abundance, [O/Fe]	$+0.56 \pm 0.08$	(8)
Rotational velocity, $v \sin i$	2.4 km s^{-1}	(8)
V	5.166 ± 0.014	(9)
$B - V$	0.695 ± 0.006	(9)

Note.
[a] Sources: (1) this paper, Table 7; (2) Boyajian et al. 2008, adjusted for parallax; (3) Heiter et al. 2015, adjusted for parallax; (4) this paper, calculated from L and R, and assuming a solar $T_{\rm eff} = 5771 \pm 1$ K from Heiter et al.; (5) this paper, calculated from M and R; (6) Jofré et al. 2014, 2018; (7) mean of Mg, Si, Ca, and Ti, from Jofré et al. 2018; (8) Luck 2017, C and O abundances converted from his [C/H] and [O/H] values using his [Fe/H] = −0.75; (9) combined light of AB system, from Mermilliod 1991.

Rows 6–9 of Table 9 summarize the chemical composition (see Section 8.2). Row 10 gives the rotational velocity, $v \sin i$. The final two rows of the table give the V magnitude and $B - V$ color of the μ Cas system, from the literature compilation by Mermilliod (1991).

As noted by B08, the effective temperature, luminosity, and radius of μ Cas A are approximately those of a normal Population I K0 V dwarf, and we now see that this is also true of the mass. The fact that the star had been considered to be a standard star with an earlier spectral type of G5 V (e.g., Keenan & Keller 1953) is a result of the metallic-line weakening caused by the star's metal deficiency, [Fe/H] = −0.81.

Less than half a dozen field late-type dwarfs as metal deficient as μ Cas A have had dynamical-mass determinations (e.g., Jao et al. 2016). Of these, the mass of μ Cas A now has by far the highest precision. Precise masses and radii have also been derived for the components of several eclipsing binaries in metal-poor globular clusters (GCs; Thompson et al. 2020, and references therein).

9. Astrophysical Implications

As outlined in the previous section, there remain uncertainties in the effective temperature and other parameters of μ Cas A. Moreover, we have raised a possible concern about the measurement of its angular diameter (Section 8.1). Effective temperatures near $T_{\rm eff} = 5340$ K have been found in many spectroscopic and photometric studies, but somewhat higher temperatures are generally found from application of the IRFM. A significant increase in the adopted temperature of μ Cas A would certainly impact, e.g., the metallicity of [Fe/H] =−0.81 (see Table 9), which was derived assuming $T_{\rm eff} = 5308$ K and LTE conditions. As a rule of thumb, increasing the temperature by 100 K will result in about a 0.1 dex increase in the [Fe/H] value derived from Fe I lines—although metallicities based on Fe II lines are known to be much less sensitive to $T_{\rm eff}$. Fortunately, corrections for non-

LTE effects appear to be small for stars with intrinsic properties (temperatures, gravities, and metallicities) similar to those of μ Cas A ($\lesssim$0.02 dex, according to Lind et al. 2012; see their Figure 2).

Since the effective temperature and diameter of μ Cas A remain uncertain, it is not possible to constrain its age and helium abundance as tightly as we had hoped—inspired by D65—when we began our HST program. Nevertheless, with reasonable assumptions for its $T_{\rm eff}$ and metallicity, together with the considerably improved mass precision that is the main result of our study, comparisons of theoretical predictions for the mass–radius and mass–luminosity diagrams with the observed quantities can be made. These should provide some indication whether μ Cas A has close to the primordial helium abundance ($Y_p \approx 0.247$; see Cyburt et al. 2016). We should also be able to make an improved estimate of the star's age. Previous age determinations for μ Cas A have varied remarkably widely, from about 2–3 to 11 Gyr (e.g., Nordström et al. 2004; Mamajek & Hillenbrand 2008; Luck 2017).

Rather than adopting, say, the mean $T_{\rm eff}$ and [Fe/H] values from recent publications, which may or may not be entirely consistent with each other, we decided to rely on photometric observations of μ Cas A, subject to constraints provided by the GC 47 Tucanae. We will also take into account the interferometric angular diameter (B08), our updated parallax (Table 4), and our new precise mass determination (Table 7).

The main role of 47 Tuc in our discussion below is to calibrate the transformations between $B-V$ and $T_{\rm eff}$ and thereby tie our results for the field metal-poor star μ Cas A to its counterparts in a GC with nearly the same metallicity, and presumably a similar age. We were motivated to do this because we noticed that μ Cas A is intrinsically redder than MS stars in 47 Tuc at the same absolute magnitude, which is the opposite of what is expected if the star is slightly more metal-poor than the cluster, as indicated by most [Fe/H] determinations. Importantly, this approach ensures that the properties of μ Cas A are derived in a fully consistent way, although the accuracy of our findings in an absolute sense will depend on various factors, including, in particular, the assumed radius and adopted $B-V$ color of μ Cas A and the photometry, metallicity, and reddening of 47 Tuc. Consistent with the $E(B-V)$ value that is obtained from the three-dimensional extinction maps of Capitanio et al. (2017),[11] we will assume that μ Cas is unreddened.

9.1. Constraints from 47 Tucanae

Figure 7 shows where μ Cas A is located relative to MS stars in the color–magnitude diagram (CMD) of 47 Tuc, which is assumed to have the apparent distance modulus and reddening that are specified in the lower left corner of the plot. (We have used the cluster photometry that is publicly available in P. B. Stetson's "Homogeneous Photometry" archive;[12] these observations are discussed by Bergbusch & Stetson 2009.) Brogaard et al. (2017) studied the available determinations of the foreground reddening of the cluster and concluded that $E(B-V) = 0.03 \pm 0.01$ is the current best estimate. This value differs from the mean values derived from dust maps (Schlegel et al. 1998; Schlafly & Finkbeiner 2011; Capitanio et al. 2017) by only 0.002–0.004 mag.

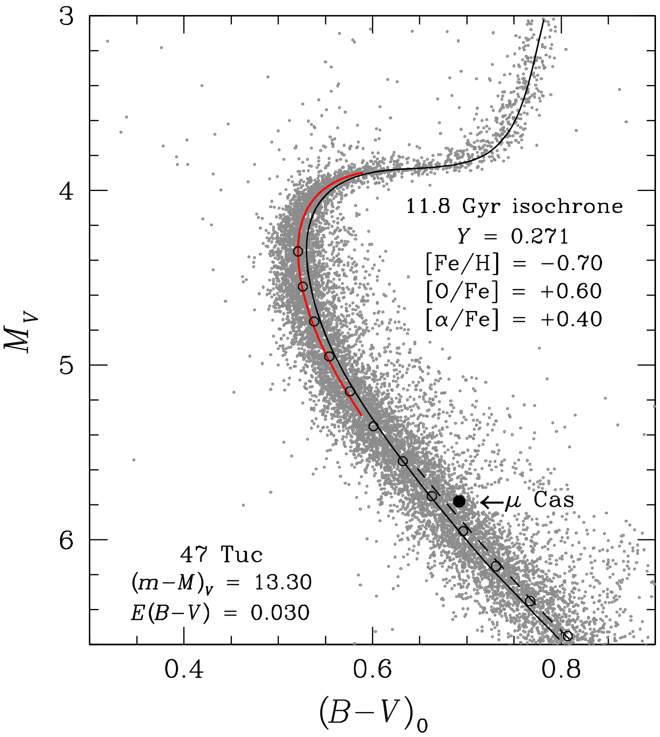

Figure 7. Comparison of the locations of μ Cas A and MS stars in 47 Tucanae in the $[(B-V)_0, M_V]$-diagram. Plotted as open circles are median points that were derived from the binning of the cluster stars in intervals of 0.2 mag in V. The solid curve in black represents an 11.8 Gyr isochrone for the indicated chemical abundances, where [α/Fe] includes all of the α-elements except oxygen, which is specified explicitly. If this isochrone is adjusted by $\delta(B-V) = 0.009$ mag to the blue, it reproduces the observed TO luminosity, as shown by the red curve. (For clarity, only the TO portion of the latter is plotted.) The dashed curve shows where the lower MS of an otherwise identical isochrone to the solid black curve, but for the helium content lowered to $Y = 0.25$, would be located.

The distance moduli for 47 Tuc that have been derived in recent studies, using independent methods, are also in superb agreement. Brogaard et al. used the eclipsing-binary member V69 to obtain $(m-M)_V = 13.30 \pm 0.06$, which happens to be midway between the values of 13.27 from simulations of the horizontal branch (HB) population of 47 Tuc (Denissenkov et al. 2017) and 13.33 from Gaia DR2 parallaxes (Chen et al. 2018), both of which have similar uncertainties. The latter estimate, which used background stars in the Small Magellanic Cloud and quasars to account for spatial and magnitude variations of the parallax zero-point (see Lindegren et al. 2018), is particularly noteworthy because it is model independent.

We determined the position of μ Cas A plotted in Figure 7 as follows. According to the compilation by Mermilliod (1991), which tabulates homogeneous mean photometry in the *UBV* system, μ Cas has $V = 5.166 \pm 0.014$ and $B-V = 0.695 \pm 0.006$. Its distance of 7.54 pc, calculated from our adopted parallax (Table 4), corresponds to a true distance modulus of $(m-M)_0 = -0.614$. From this we obtain $M_V = +5.78$. The photometric properties of μ Cas A itself will be slightly different because of the presence of the low-mass companion (see Table 7). Its contribution can be estimated by determining its absolute magnitudes in the B and V bandpasses from stellar models for its measured mass and the metallicity of the system. Subtracting these contributions from the observed luminosities, we find $V \simeq 5.170$ and $B-V \simeq 0.692$ for μ Cas A. Even though the bolometric corrections (BCs) applicable to very low

---

[11] http://stilism.obspm.fr

[12] www.cadc.hia.nrc.gc.ca/en/community/STETSON/homogeneous

mass stars have significant uncertainties, the effects of the companion on the observed photometry amount to no more than a few thousandths of a magnitude.

Superimposed on the CMD in Figure 7 is an 11.8 Gyr isochrone for the indicated chemical abundances. It has been transposed from the theoretical to the observed plane using the color–$T_{\rm eff}$ relations given by Casagrande & VandenBerg (2014). This is the same isochrone used by Brogaard et al. (2017) to fit both the turnoff (TO) photometry of 47 Tuc and the properties of the eclipsing binary V69. Were it not for the binary, it would be difficult to argue against the possibility that 47 Tuc has a lower metallicity or reduced abundances of oxygen and/or the other α-elements. In addition, according to Denissenkov et al. (2017), the distribution of HB stars in 47 Tuc can be reproduced very well by synthetic HBs if there is a star-to-star variation of the initial He abundance by $\Delta(Y) \simeq 0.03$, with a mean abundance corresponding to $\langle Y \rangle \simeq 0.271$. Cluster MS stars with this He abundance are therefore assumed to lie along the median fiducial sequence that has been plotted as open circles.[13] The dashed curve, which represents the lower MS portion of an isochrone for the same age and metal abundances, but with the helium content reduced to $Y = 0.250$, serves to illustrate the dependence of predicted MS loci on Y.

There are systematic differences between the isochrone and the median cluster fiducial, in the sense that the models are too red by about 0.01 mag in the vicinity of the TO and by a similar amount, but in the opposite sense, at $M_V = +6.6$. However, the predicted $B - V$ colors at the absolute magnitude of μ Cas A are too blue by only 0.003 mag. Although this offset is quite small, it should (and will) be taken into account when we fit isochrones to the photometric properties of μ Cas A. Thus, we have learned from our study of 47 Tuc that the $B - V$ colors that are derived from the tables of BCs given by Casagrande & VandenBerg (2014) should be adjusted to the red by 0.003 mag when applied to stars with properties similar to those of μ Cas A. To be sure, many assumptions have been made in reaching this point, such as the reddening and the helium and metal abundances of 47 Tuc, but the best estimates of the various parameters result in μ Cas A lying slightly to the red of the cluster MS. The goal of our analysis now is to understand why that is, and what the implications are for the properties of μ Cas A.

Having established the absolute V magnitude of μ Cas A and its $B - V$ color, we can use our tables of BCs to convert M_V to $M_{\rm bol}$, and thence to the bolometric luminosity. The BC tables require input values of $T_{\rm eff}$ and [Fe/H]. (They also depend on [α/Fe], but we have opted to assume that $[\alpha/{\rm Fe}] = +0.3$, given the support for this value from observational studies; see Table 9.) Since the luminosity can also be calculated from the radius and $T_{\rm eff}$, it is necessary to iterate on the input parameters until (1) both ways of calculating the luminosity yield the same result and (2) the predicted $B - V$ color (including the small offset described above) matches the observed color. With just a few iterations of this procedure, we obtained $[{\rm Fe/H}] = -0.74$, $T_{\rm eff} = 5346$ K, and $L/L_\odot = 0.458$. (We have assumed that this temperature has an uncertainty of ±70 K, mainly so that the error bar encompasses the effective temperatures derived from both interferometric studies and the IRFM. For the luminosity uncertainty, we have adopted $\pm 0.014\,L_\odot$, which corresponds to a 0.03–0.035 mag uncertainty of our BCs.) Remarkably, this temperature is within a few kelvin of the mean spectroscopic and photometric determinations tabulated by Heiter et al. (2015), and the metallicity is within 0.07 dex of the values given by Heiter et al. and Luck (2017). Our determination of the luminosity is within 1σ of the value of $L/L_\odot = 0.445 \pm 0.005$ given by Heiter et al. (our Table 9). As we have adopted B08's determination of the diameter of μ Cas A in our analysis but found a higher temperature by ≈50 K, the bolometric flux that B08 derived must be smaller than our estimate.

The problem remains that the photospheric metallicity of μ Cas A appears to be lower than that of 47 Tuc, and yet it is redder than cluster stars of the same absolute magnitude. This is very likely the consequence of diffusive processes. It is now well established that diffusion acts to reduce the abundances of He and the metals in the surface layers of old stars, although extra mixing below surface convection zones must also be present to limit the efficiency of gravitational settling. Otherwise, as shown by Richard et al. (2002), diffusive models would be unable to explain the observed variation of the Li abundance with $T_{\rm eff}$ in the so-called "Spite-plateau" stars (Spite & Spite 1982) or the abundance variations between the TO and lower red giant branch (RGB) in GCs.

In the lowest-metallicity GCs, such as NGC 6397, observations have revealed that the difference in metallicity between the TO and lower RGB is about 0.15 dex (Korn et al. 2007; Nordlander et al. 2012), which is in rather good agreement with the expectations from diffusive stellar models with extra mixing (see VandenBerg et al. 2002, their Figure 9, concerning the very metal-deficient cluster M92). At intermediate metallicities, the variation in [Fe/H] appears to be somewhat less; e.g., Gruyters et al. (2014) have found a difference of about 0.1 dex across the subgiant branch. Marino et al. (2016) found an even smaller difference in 47 Tuc, although the uncertainties are such that the variation could be anywhere in the range from 0.0 to 0.1 dex. Part of the difficulty is that the difference in [Fe/H] between the TO and RGB is quite dependent on the assumed $T_{\rm eff}$ scale (see Gruyters et al. 2014, their Table 5). Regardless, the signature of diffusion appears to have been detected in the near-solar-abundance open cluster M67 as well (Önehag et al. 2014; Bertelli Motta et al. 2018), but its effects are much smaller ($\Delta[{\rm Fe/H}] \simeq 0.04$–$0.05$ dex), probably due mostly to its considerably younger age.

In any case, it is reasonable to assume that [Fe/H] values for μ Cas A that are derived from spectroscopic or photometric studies should be increased by about 0.08 dex in order to obtain the metallicity that applies to its interior structure. Therefore, the isochrones that are used to interpret the observations of this star should assume $[{\rm Fe/H}] \approx -0.66$. Indeed, it is this value of [Fe/H] that should be compared with the metallicity of 47 Tuc that has been inferred from the binary V69, because that is the relevant metal abundance for the calculation of the mass–radius and mass–luminosity relations that are used in comparisons with the measured masses and radii and the derived luminosities of the components of the binary. By the same token, the surface metallicities of upper-MS stars in 47 Tuc should be less than that of μ Cas A. Clearly, a small difference in [Fe/H], with 47 Tuc being more metal-poor than μ Cas, would help to explain the small offset of the latter relative to cluster MS stars of the same

---

[13] As discussed by VandenBerg et al. (2013), the best estimate of the TO age is obtained by first shifting in the horizontal direction all of the isochrones for a suitable range in age until each of them matches the observed TO color, and then determining which one provides the best superposition of the subgiant stars located just past the TO. Figure 7 shows that if the isochrone in black were adjusted to the location of the red curve, it would provide a good fit to the TO and subgiant stars. The advantage of this procedure is that errors in predicted or observed colors have little or no impact on the derived age.

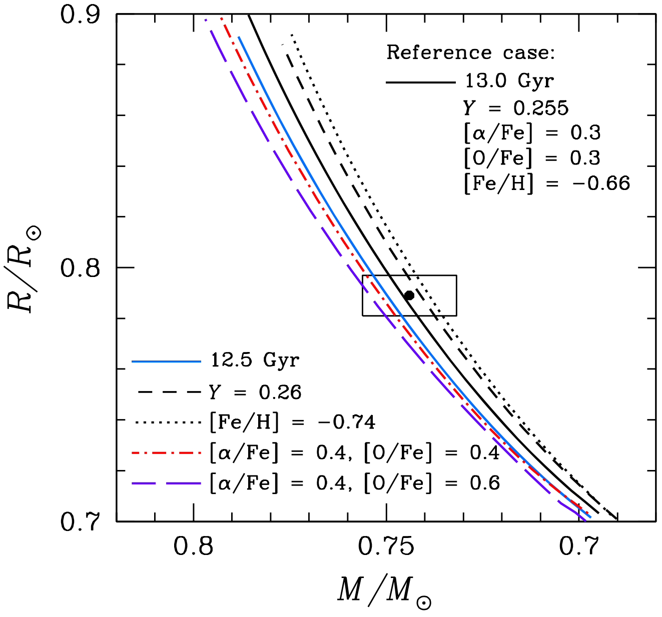

Figure 8. Comparison of predicted mass–radius relations from isochrones for the indicated ages and chemical abundances with the mass and radius of μ Cas A (filled circle and error box). The black solid curve represents the reference case; the others illustrate the effects of varying the age, Y, and the metal abundances, in turn, as indicated in the lower left corner. The various abundance choices correspond to initial chemical compositions. Due to the operation of diffusive and extra mixing processes since μ Cas formed, it is expected that its surface metallicity and He abundance will have changed by Δ[Fe/H] ≈ -0.08 dex and $\Delta Y \approx -0.03$, respectively (see the text). Note that colors are not affected by the modest variations in the atmospheric abundance of helium that are predicted to occur during MS evolution.

M_V on the [$(B-V)_0$, M_V]-diagram. A difference in the He abundance may also be partly responsible for the difference in color (note in Figure 7 the separation of the solid and dashed curves in the vicinity of μ Cas A).[14]

In principle, spectroscopy of cluster giants should yield a metallicity that is close to the initial metal abundance, because deepening convection along the lower RGB will dredge back into the surface layers most (but not all) of the helium and the metals that had settled into the interior during the core H-burning phase, i.e., the effects of diffusion are mostly erased during the evolution along the lower RGB. However, due mainly to systematic uncertainties, it is difficult to derive absolute metal abundances to within ∼0.1 dex. Although, for instance, the new metallicity scale developed by Carretta et al. (2009) gives [Fe/H] = −0.76 for 47 Tuc, higher or lower values by 0.05 to 0.1 dex are commonly found (e.g., Cordero et al. 2014; Wang et al. 2017; Thygesen et al. 2018).

9.2. The Age and Helium Abundance of μ Cas

Using our adopted or derived properties for μ Cas A, we can now consider their implications for its age and helium content. Figure 8 shows the observed mass and radius of the star and the associated error bars (the filled circle and error box) and superposes the predicted mass–radius relations from several isochrones. The latter were generated from the grids provided by VandenBerg et al. (2014), with the exception of a set of models that was computed for [O/Fe] = +0.6, using the same stellar evolutionary code. Unfortunately, we can produce models only for [α/Fe] = [O/Fe] = +0.3 and +0.4, and for [O/Fe] = +0.6 when [α/Fe] = +0.4 is adopted for the other α-elements (due to the lack of low-temperature opacities for other mixtures of the metal abundances). The solid curve, as defined in the legend in the upper right corner of the figure, represents the adopted reference case, while the others (see legend in the lower left corner) assume all of the same parameter values except for the changes that are given explicitly. The figure shows that models for high ages and low values of Y provide good fits to the observed properties of μ Cas A. This is not surprising, given that a metal-poor, high-velocity star in the solar neighborhood is likely to have formed early in the evolution of the Milky Way.

The solid blue curve in Figure 8 shows the effect of reducing the age of the star by 0.5 Gyr. Lower ages imply higher masses, i.e., the predicted *M–R* relation is shifted to the left. The differences between the reference curve and the dashed locus illustrate the consequences of increasing the He abundance by $\Delta Y = 0.005$; higher Y results in a lower mass at a fixed radius. A similar, but somewhat larger, offset (in the same direction) is obtained if the adopted [Fe/H] value is reduced by 0.08 dex; compare the location of the reference curve with that of the dotted curve. In addition, the location of the dotted–dashed locus relative to the reference case shows the effect of increasing the α-element abundances from [α/Fe] = +0.3 to +0.4. In this case, the predicted *M–R* relation is shifted to higher masses, which also occurs if the assumed oxygen abundance is increased by 0.2 dex; compare the dotted–dashed and long-dashed curves.

An age of 13.0 Gyr was assumed for most of the isochrones, because this estimate is close to the maximum possible age of μ Cas, given that the big bang apparently occurred about 13.8 Gyr ago (Bennett et al. 2011; Planck Collaboration et al. 2014). Although the predicted mass–radius relation that applies to μ Cas A could be slightly to the right of those that have been plotted—which is the direction of increasing age—it is perhaps somewhat more probable that the relevant relation is located somewhat to the left. The permitted age range therefore depends on how far the predicted *M–R* relation is from the lower left corner of the error box. For instance, for the cases plotted as dotted–dashed and long-dashed curves, the mass–radius relations for ages less than 11.5–12.0 Gyr would lie outside the error box.

Obviously, the uncertainties can accommodate much larger ranges in age if a higher He abundance or a lower metallicity is assumed, since these cases (the dashed and dotted loci) are located farther to the right than any of the others. In fact, although the isochrones were generated for He abundances in the range $0.25 \leqslant Y \leqslant 0.26$, there is ample room within the error box that, e.g., the dotted–dashed and long-dashed cases could be made to satisfy the observational constraints for ages well below 11 Gyr, provided that the assumed He abundance is increased by a sufficient amount. According to Figure 8, an increase in Y by 0.005 has almost the same effect on the mass–radius relation as an increase in age by 0.5 Gyr, that is, such changes, if made simultaneously to the models, result in essentially the same relation between mass and radius. Thus, the current uncertainties associated with the mass and radius of μ Cas A can potentially accommodate a fairly large range in Y and age (although it would be very surprising if this star has $Y > 0.26$).

---

[14] As noted by the referee, the formation and early evolution of a binary star occur in a very different environment than in the case of an isolated, single star. It is possible that this could give rise to small differences in their CMD properties at the same mass, age, and chemical composition.

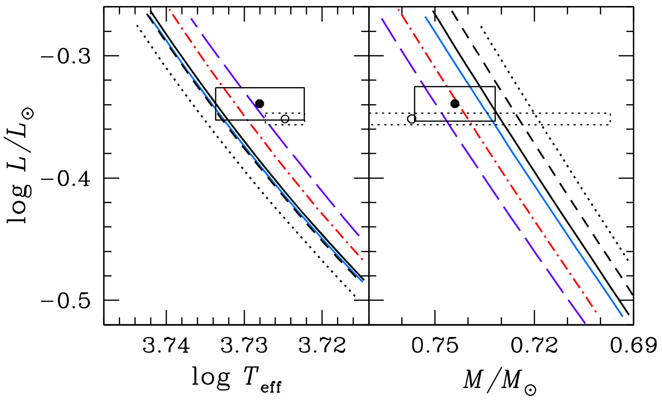

Figure 9. Isochrones from the previous figure, with the same color and line-type encoding, except that comparisons with the properties of μ Cas A are made on the H-R diagram (left panel) and the mass–luminosity diagram (right panel). The filled circles and solid error boxes show our measured and adopted values. The open circles and dotted error boxes represent the $T_{\rm eff}$ and luminosity that were derived by Boyajian et al. (2008) and Heiter et al. (2015), respectively (but corrected for our adopted parallax), along with the best estimate of the mass of μ Cas A before the present study, $0.757 \pm 0.060\,M_\odot$ (from Lebreton et al. 1999).

Figure 9 compares the same isochrones with the observed properties of μ Cas A on the H-R diagram and the mass–luminosity plane. In these two panels, we plot μ Cas A at $L = 0.458 \pm 0.014\,L_\odot$ and $T_{\rm eff} = 5346 \pm 70$ K from the discussion in Section 9.1 and at the dynamical mass of $0.7440 \pm 0.0122\,M_\odot$ determined in this paper. We use filled circles and solid lines for the associated error boxes for these results. To compare with earlier results, we use open circles and dotted error boxes to plot the location of the star based on the $T_{\rm eff}$ from B08 and the luminosity from Heiter et al. (2015) (both slightly adjusted to take our revised parallax into account) and the mass from Lebreton et al. (1999), which was acknowledged by B08 to be the best available one at the time. Interestingly, the dashed locus (which assumed a helium content of $Y = 0.26$) is significantly displaced from the observations in both panels, whereas it provided quite a good fit to the observed mass and radius in the previous figure.[15] The discrepancy is even larger if the dashed curve is compared with the open circles. However, predicted M–L relations should be more robust than those that involve temperatures or radii, because the latter are subject to many uncertainties, including the treatment of convection and the atmospheric boundary condition. On the other hand, our models generally provide good fits to GC CMDs, especially to the morphologies of their MS stars (see, e.g., the plots provided by VandenBerg et al. 2014; Casagrande & VandenBerg 2014), which suggests that the model $T_{\rm eff}$ scale is reasonably good.[16]

Although the dotted–dashed curve appears to provide the best consistency between the models and our results for μ Cas A (the filled circle) in the mass–luminosity plane, it does not take into account the relatively high abundance of oxygen. In addition, the assumed abundances of the other α-elements are slightly too high (see Table 10). If the reasonable assumption is made that oxygen and iron diffuse at a similar rate, the initial and current [O/Fe] values will be about the same; consequently, the models that are compared with the observations should assume $[{\rm O/Fe}] = +0.56$. We can evaluate how much the predicted M–L relations would be affected by such an oxygen enhancement, using the data that are listed in Table 10. This gives the masses that are obtained by interpolation along the computed M–R and M–L relations at, in turn, the observed radius ($0.789\,R_\odot$) and the luminosity that we have derived ($\log L/L_\odot = -0.339$). The last two numbers in the right-hand column tell us that $\Delta[{\rm O/Fe}] = +0.2$ will increase the predicted mass by $0.0068\,M_\odot$. Thus, a 0.26 dex increase (to be in agreement with the observed oxygen abundance) will result in a mass increased by about $0.0088\,M_\odot$, in which case the mass of our reference model would increase to $0.7420\,M_\odot$. This differs from our measured dynamical mass by only $0.0020\,M_\odot$, which is much less than its uncertainty.

However, based on the first two entries in the right-hand column of Table 10, an age reduced by 0.5 Gyr will increase the predicted mass at the derived luminosity of μ Cas A by $0.0030\,M_\odot$. Hence, the reference models will predict the observed mass if the assumed oxygen abundance is increased by 0.26 dex *and* the age is decreased to 12.7 Gyr. Furthermore, using the tabulated masses for the reference and the dotted–dashed cases, and taking into account the increase in mass by $0.0034\,M_\odot$ if $\Delta[{\rm O/Fe}] = 0.1$, increased abundances of all of the other α-elements, except oxygen, by $\Delta[\alpha/{\rm Fe}] = 0.1$ dex apparently increase the mass by $0.0065\,M_\odot$. Therefore, if the metal abundances of the reference model were increased by $\Delta[\alpha/{\rm Fe}] = 0.1$ and $\Delta[{\rm O/Fe}] = 0.3$, the predicted mass should increase by $0.0167\,M_\odot$ to $0.7499\,M_\odot$, which is precisely what the models predict for the long-dashed case (see Table 10). Clearly, the tabulated results are internally self-consistent.

The uncertainties of the derived age and He abundance can also be estimated using the information that is provided in Table 10. Because a reduced age by 0.5 Gyr results in a higher mass by $0.0030\,M_\odot$, the 1 σ uncertainty in the measured mass, $0.0126\,M_\odot$, is equivalent to an age uncertainty of 2.0 Gyr. In the case of the He abundance, since $\Delta Y = +0.005$ implies a mass reduced by $0.0056\,M_\odot$, the uncertainty of our mass determination corresponds to a change in Y of 0.011. However, because the predicted M–L relations are sloped, they will still pass through the lower left or upper right corners of the error box, if the mass is lower or higher than the formal uncertainty by $\approx\pm0.004M_\odot$; see Figure 9. As a result, the ranges in the age and the value of Y that are permitted by the error box are closer to ±2.7 Gyr and ±0.014, respectively. We therefore conclude that the best estimate of the age of μ Cas is 12.7 ± 2.7 Gyr and that it has a helium content of $Y = 0.255 \pm 0.014$. (Although we could carry out a similar analysis using the predicted masses that are derived from the M–R diagram, we have not done so because they would be less trustworthy than those based on the M–L diagram, for reasons already mentioned.) The low rotational velocity (Table 9) is consistent with a high age but is not decisive.

---

[15] Note, however, that the assumed metal abundances of these, or any of the other, stellar models do not correspond exactly to the observed abundances; consequently, one cannot determine the "best-fit" models simply from an inspection of Figures 8 and 9. The purpose of these two figures is to illustrate how the predicted relations between mass, radius, luminosity, and $T_{\rm eff}$ are affected when the value of each parameter (age, Y, $[\alpha/{\rm Fe}]$, etc.) is individually varied in turn. Below we show how to use the results of the model computations to derive the overall best estimates of the age and helium content of μ Cas A.

[16] Fits to BV photometry tend to be somewhat more problematic (recall the discrepancies between theory and observations in Figure 7) than in the case of VI_CK_s data (also see VandenBerg et al. 2010); consequently, the apparent difficulties with $B - V$ colors are probably due more to deficiencies in the transformations to the B bandpass than to problems with the predicted effective temperatures.

Table 10
Predicted Masses for μ Cas A for Various Stellar Models

Stellar Models (Line Type and Color)[b]	Age (Gyr)	Y	[Fe/H]	[α/Fe]	[O/Fe]	Mass ($M_\odot$)[a] at $R/R_\odot = 0.789$	Mass ($M_\odot$)[a] at $\log L/L_\odot = -0.339$
Solid (black)[c]	13.0	0.255	−0.66	+0.30	+0.30	0.7457	0.7332
Solid (blue)	12.5					0.7498	0.7362
Dashed (black)		0.260				0.7411	0.7276
Dotted (black)			−0.74			0.7388	0.7218
Dot-Dashed (red)				+0.40	+0.40	0.7514	0.7431
Long-Dashed (purple)				+0.40	+0.60	0.7542	0.7499

Notes.
[a] To be compared with the measured mass of 0.7440 $M_\odot$.
[b] Plotting line type and color used in Figures 8 and 9.
[c] First row is the "Reference" case; others assume the same parameter values except as noted.

Unfortunately, our findings remain for now more suggestive than definitive, because the published interferometric diameter of μ Cas could be too large by up to ∼8% (see Section 8.1). Although such a large correction seems unlikely, given that most spectroscopic and photometric determinations of $T_{\rm eff}$ (including ours) imply that the measured diameter is too large by only 1%–2%, it would clearly have important consequences for our understanding of μ Cas if confirmed by future work. In particular, the resultant increase in its $T_{\rm eff}$ to ∼5500 K would require a reevaluation of its metal abundances, perhaps by 0.1–0.15 dex if derived from spectroscopy. The higher temperature would be especially problematic for photometric metallicity estimates. For instance, using either the color–$T_{\rm eff}$ relations given by Casagrande & VandenBerg (2014) or the semiempirical transformations provided by Casagrande et al. (2010), the observed color, $B - V = 0.692$, would imply an [Fe/H] value $\gtrsim -0.4$. Hopefully, an effort will be made to obtain a new and improved measurement of the angular diameter of μ Cas in the near future, so that it will be possible to resolve this issue. Needless to say, any reduction in the uncertainties of its basic properties will help to improve our understanding of this important star.

10. Summary and Future Work

We have obtained high-resolution imaging of the nearby high-velocity visual binary μ Cas, using cameras on the Hubble Space Telescope over an interval of nearly two decades. By combining these data with ground-based astrometry of the binary and with ground- and space-based measurements of the parallax and photocenter motion, we have determined the orbital period (21.568 yr) and calculated dynamical masses for the two components of the binary. We find masses of $0.7440 \pm 0.0122\,M_\odot$ for the G5 V primary star, μ Cas A, and $0.1728 \pm 0.0035\,M_\odot$ for its M-dwarf companion, μ Cas B. We see no significant indication of perturbations of the HST astrometric measurements due to a third body in the system.

The main aim of our program was to determine the age and helium content of the moderately metal-poor ([Fe/H] = −0.81) primary star μ Cas A. However, although we now have a precise dynamical mass for the star, there remain issues with its other astrophysical parameters. We investigated archival interferometric measurements of its angular diameter, leading us to suspect that the diameter may have been overestimated by a few percent. Additionally, there is a fairly wide range of determinations of its effective temperature in the literature. Taking these issues into account, we estimate the age and helium content of the system to be 12.7 ± 2.7 Gyr and $Y = 0.255 \pm 0.014$. Plotting μ Cas A in the CMD of 47 Tucanae, we find that it lies at a position slightly cooler and more luminous than the cluster's MS. This is consistent with our conclusion that the star has a slightly higher age and/or lower helium content than the cluster. μ Cas is possibly the oldest star in the sky visible to the naked eye.

The dominant contributor to the error budget for the mass of μ Cas A is the uncertainty in the trigonometric parallax. It may be possible to reduce this uncertainty with Gaia observations, although the star was too bright to be included in DR2. The angular diameter measurement could be improved using CHARA observations in the V or H bands. It would be important also to reconcile the various determinations of the effective temperature and to redetermine the chemical composition based on consistent atmospheric parameters.

This work was inspired by the classical paper of Dennis (1965). We are closer now to achieving his goal of a precise helium content for this ancient metal-poor star, with its cosmological implications, but further work remains to be done.

We are indebted to the numerous observers who painstakingly accumulated data on this difficult and important star over several decades. Support was provided by NASA through grants from the Space Telescope Science Institute, which is operated by the Association of Universities for Research in Astronomy, Inc., under NASA contract NAS5-26555. G.H.S. acknowledges support from NSF grant AST-1636624. We thank the referee for urging us to consider the effects of CTI in the WFPC2 images. Useful comments and unpublished data were provided by J. Drummond, G. Gatewood, L. Roberts, and J. Russell. Randal Telfer provided important information related to chromatic aberration in the WFC3 camera. Advice and support during the planning, execution, and analysis of the HST observations were provided by STScI Contact Scientists, Program Coordinators, and staff members: S. Baggett, J. Biretta, G. Hartig, R. Lucas, J. Mack, T. Royle, E. Sabbi, K. Sahu, D. Taylor, and A. Vick. We thank Bengt Gustafsson for helpful comments on chemical abundance determinations.

Facilities: CHARA, Gaia, Hipparcos, HST (WFPC2, WFC3).

Appendix A
Correcting for Charge Transfer Inefficiency in HST WFPC2 F953N Images

As described in Section 3.1, we found evidence for CTI-induced positional offsets in our WFPC2 astrometry, at a level

Table 11
Uncorrected WFPC2/F953N Astrometric Measurements of μ Cas B Relative to μ Cas A

UT Date	Besselian Date	Separation (arcsec)	J2000 Position Angle (deg)
1997 Jul 04	1997.5057	0.4189 ± 0.0010	226.391 ± 0.092
1998 Jan 02	1998.0047	0.4454 ± 0.0009	214.246 ± 0.066
1998 Jul 22	1998.5544	0.4077 ± 0.0002	200.461 ± 0.075
1999 Feb 28	1999.1612	0.3490 ± 0.0004	179.567 ± 0.087
1999 Aug 04	1999.5906	0.3150 ± 0.0007	160.830 ± 0.101
2000 Feb 01	2000.0868	0.3226 ± 0.0006	136.991 ± 0.071
2000 Jul 15	2000.5390	0.3624 ± 0.0005	118.189 ± 0.064
2001 Jan 15	2001.0406	0.4324 ± 0.0004	102.605 ± 0.067
2001 Jul 30	2001.5773	0.5224 ± 0.0003	91.290 ± 0.057
2002 Jan 17	2002.0476	0.6119 ± 0.0004	84.426 ± 0.040
2002 Aug 05	2002.5934	0.7085 ± 0.0003	78.491 ± 0.059
2003 Feb 11	2003.1144	0.8049 ± 0.0003	74.159 ± 0.036
2003 Aug 05	2003.5942	0.8838 ± 0.0006	70.919 ± 0.036
2004 Jan 29	2004.0772	0.9662 ± 0.0002	68.329 ± 0.037
2004 Aug 08	2004.6039	1.0403 ± 0.0006	65.848 ± 0.040
2005 Jan 15	2005.0412	1.1087 ± 0.0003	64.165 ± 0.035
2005 Aug 13	2005.6175	1.1796 ± 0.0005	61.853 ± 0.035
2006 Jan 30	2006.0815	1.2400 ± 0.0003	60.490 ± 0.035
2006 Sep 26	2006.7400	1.3014 ± 0.0004	58.610 ± 0.034
2007 Oct 17	2007.7933	1.3887 ± 0.0003	55.856 ± 0.032

reaching about 5 mas toward the end of WFPC2's lifetime. To compensate for this effect, we added a final analysis step for the WFPC2 measurements, involving an empirical characterization of possible CTI effects. We describe these corrections in this appendix.

The WFPC2 observations covered 10.3 yr, reaching nearly the end of the instrument lifetime, when CTI losses had become largest. CTI is expected to grow roughly linearly in time and primarily affects inferred positions of faint objects through distortion of the PSF in the detector's y-direction, which is the direction of charge readout. Our WFPC2 observations happened to be well posed for empirically determining astrometric CTI effects, with many observations being taken about 6 months apart, at telescope orientations differing by about 180°.

We derived right ascension and declination residuals from an initial orbital fit to the motion of μ Cas B around A. These showed a signature of alternating residuals, especially in R.A., that were correlated with telescope roll angle and growing with time. We transformed the residuals into detector x, y deviations. These deviations were then fit to linear functions of time. The fit to the x deviations was not statistically significant, with a 30% chance that random variations could explain the linear correlation. In y, however, where CTI is expected to influence position determinations, there was only a 0.8% chance that the derived linear correlation could result from random errors. A least-squares fit yielded a progressive shift in y of 0.12 pixels over the 10.3 yr observing baseline (equivalent to a shift in y reaching $0\overset{''}{.}0054$ at the end of the 10.3 yr interval). We applied these corrections to the astrometry and then transformed the x, y positions back to R.A. and decl., and then to position angle and separation. The CTI-adjusted WFPC2 astrometry is listed in the first 20 lines in Table 2. Application of this CTI correction eliminated the previously noted alternating deviations in R.A. and dropped the residual scatter by about a factor of two.

For reference, Table 11 lists the WFPC2 astrometry we obtained before making the CTI corrections.

Appendix B
Correcting for Chromatic Aberration in HST WFC3 F225W Images

As discussed in Section 3.2, we found it necessary to make corrections to our astrometric measurements of the μ Cas binary that were made on frames obtained in the HST WFC3 F225W bandpass. Although the WFC3 camera primarily uses reflective optics, the color filters and front windows of the CCD module are transmissive elements. Thus, there is a small amount of chromatic aberration in the camera. To compensate for this, the thicknesses of the filters were adjusted to maintain confocality and a common plate scale, at the nominal wavelength of each filter. This approach becomes an important problem in the case of μ Cas, because there is a significant red leak in the F225W filter, combined with the fact that μ Cas B is an M dwarf, which is considerably redder than the G-type primary star.

To assess the size and direction of this effect in the HST images, we first obtained the system throughput curve of the camera plus F225W filter from the WFC3 website[17] at the Space Telescope Science Institute (STScI). We convolved this with the spectral energy distributions for stars of spectral types G8 V and M4 V, taken from the observational stellar-flux library assembled by Pickles (1998); these are also conveniently available from STScI.[18] This convolution shows that the flux from μ Cas B is almost entirely detected through the red leak of the F225W filter. We find an effective wavelength for the B component of about 8600 Å. Even the detected light from μ Cas A is mostly at the long-wavelength side of the filter's main bandpass; we find an effective wavelength for the A component of about 2500 Å.

We are grateful to Randal Telfer, Astronomical Optics Scientist at STScI, for providing us with information on the differential chromatic aberration in WFC3 images, from which we calculated approximate corrections to be applied to our astrometry. The dispersion induced by the windows and filter has two effects: (1) an overall shift in image position across the field due primarily to a small tilt in the detector windows, and (2) an increase in magnification at longer wavelengths. The size of these effects is predictable, using the known wavelength dependence of the index of refraction of fused silica.

For the image offset, Telfer provided a tabulation for the F225W filter as a function of wavelength. The offsets in detector x, y coordinates increase from zero at the filter's central wavelength, to $(\Delta x, \Delta y) = (-0.008, +0.091)$ pixels at 2500 Å and $(-0.037, +0.407)$ pixels at 9000 Å. By interpolating in the table to the effective wavelengths for μ Cas A and B, we find a net offset of the B image relative to A of $(\Delta x, \Delta y) = (-0.025, +0.271)$ pixel.

The effect of the higher magnification at longer wavelengths is to move the image of B in the direction away from the center of the detector relative to the position of the bluer A component. By interpolation in the tabulation of magnification versus wavelength, we find a difference in magnification between that for B and A of 0.00052.

---

[17] http://www.stsci.edu/hst/instrumentation/wfc3/performance/throughputs

[18] https://ssb.stsci.edu/cdbs_open/cdbs/deliveries/etc/trds.24.3xxxx/grid/pickles/dat_uvk/

Table 12
Uncorrected WFC3/F225W Astrometric Measurements of μ Cas B Relative to μ Cas A

UT Date	Besselian Date	Separation (arcsec)	J2000 Position Angle (deg)
2010 Jan 09	2010.0236	1.4730 ± 0.0037	50.142 ± 0.073
2010 Dec 03	2010.9222	1.4926 ± 0.0056	50.046 ± 0.283
2011 Dec 05	2011.9264	1.4464 ± 0.0017	47.613 ± 0.075
2012 Dec 02	2012.9204	1.3590 ± 0.0010	45.046 ± 0.098
2013 Oct 25	2013.8179	1.2262 ± 0.0007	43.050 ± 0.125
2015 Jan 06	2015.0150	1.0372 ± 0.0007	38.375 ± 0.080

Combining these, the differential offset of B relative to A in pixels becomes

$$\Delta x = -0.025 + 0.00052\,(x - x_0),$$
$$\Delta y = +0.271 + 0.00052\,(y - y_0),$$

where (x, y) is the pixel position of the star and (x_0, y_0) is the pixel position of the center of the detector, nominally (2048, 2048) pixels.

For the F225W observation in 2010 January, we used the UVIS1-M512-SUB subarray, placing the stars at nominal position $(x, y) = (2048, 2304)$ and resulting in an offset of μ Cas B relative to A of $(\Delta x, \Delta y) = (-0.025, +0.404)$ pixels. The rest of our F225W data used the UVIS2-C512C-SUB subarray, nominally centered at $(x, y) = (256, 256)$. At this location, the relative offset is $(\Delta x, \Delta y) = (-0.957, -0.661)$ pixels. In arcseconds the offsets are small, $(-0\overset{\prime\prime}{.}001, +0\overset{\prime\prime}{.}016)$ for the first 2010 observation and $(-0\overset{\prime\prime}{.}038, -0\overset{\prime\prime}{.}026)$ for the rest, but they are large compared to the precision of the HST astrometry.

Table 12 lists the astrometric measurements of μ Cas B before applying the above corrections. The (x, y) positions on the detector have been converted to separation and P.A. on the sky, using the known plate scale and orientation of the spacecraft, as described in Section 3. These values, adjusted for chromatic aberration, are included in the main text, in Table 2.

ORCID iDs

Howard E. Bond https://orcid.org/0000-0003-1377-7145
Gail H. Schaefer https://orcid.org/0000-0001-5415-9189
Ronald L. Gilliland https://orcid.org/0000-0002-1554-5578
Don A. VandenBerg https://orcid.org/0000-0003-3277-7685

References

Abt, H. A., Sanwal, N. B., & Levy, S. G. 1980, ApJS, 43, 549
Abt, H. A., & Willmarth, D. 2006, ApJS, 162, 207
Abt, H. A., & Willmarth, D. W. 1987, ApJ, 318, 786
Adams, W. S., & Joy, A. H. 1919, ApJ, 49, 179
Agati, J.-L., Bonneau, D., Jorissen, A., et al. 2015, A&A, 574, A6
Bach, K. 2015, JKAS, 48, 165
Beavers, W. I., & Eitter, J. J. 1986, ApJS, 62, 147
Bennett, C. L., Larson, D., Weiland, J. L., et al. 2011, ApJS, 208, 20
Bergbusch, P. A., & Stetson, P. B. 2009, AJ, 138, 1455
Bertelli Motta, C., Pasquali, A., Richer, J., et al. 2018, MNRAS, 478, 425
Bond, H. E., Gilliland, R. L., Schaefer, G. H., et al. 2015, ApJ, 813, 106, (B15)
Bond, H. E., Gilliland, R. L., Schaefer, G. H., et al. 2018, RNAAS, 2, 147
Bond, H. E., Schaefer, G. H., Gilliland, R. L., et al. 2017, ApJ, 840, 70, (B17)
Boyajian, T. S., McAlister, H. A., Baines, E. K., et al. 2008, ApJ, 683, 424, (B08)
Brogaard, K., VandenBerg, D. A., Bedin, L. R., et al. 2017, MNRAS, 468, 645
Campbell, W. W. 1901, ApJ, 13, 98
Capitanio, L., Lallement, R., Vergely, J. L., Elyajouri, M., & Monreal-Ibero, A. 2017, A&A, 606, A65
Carretta, E., Bragaglia, A., Gratton, R. G., D'Orazi, V., & Lucatello, S. 2009, A&A, 508, 695
Casagrande, L., Portinari, L., Glass, I. S., et al. 2014, MNRAS, 439, 2060
Casagrande, L., Ramírez, I., Meléndez, J., Bessell, M., & Asplund, M. 2010, A&A, 512, 54
Casagrande, L., & VandenBerg, D. A. 2014, MNRAS, 444, 392, (CV14)
Casamiquela, L., Tarricq, Y., Soubiran, C., et al. 2020, A&A, 635, A8
Chen, S., Richer, H., Caiazzo, I., & Heyl, J. 2018, ApJ, 867, 132
Christou, J. C., & Drummond, J. D. 2006, AJ, 131, 3100
Cordero, M. J., Pilachowski, C. A., Johnson, C. I., et al. 2014, ApJ, 780, 94
Cyburt, R. H., Fields, B. D., Olive, K. A., & Tsung-Han, Y. 2016, RvMP, 88, 015004
Denissenkov, P. A., VandenBerg, D. A., Kopacki, G., & Ferguson, J. W. 2017, ApJ, 849, 159
Dennis, T. R. 1965, PASP, 77, 283, (D65)
Drummond, J. D., Christou, J. C., & Fugate, R. Q. 1995, ApJ, 450, 380
Duquennoy, A., Mayor, M., & Halbwachs, J.-L. 1991, A&AS, 88, 281
Faulkner, J. 1971, PhRvL, 27, 206
Feibelman, W. A. 1976, ApJ, 209, 497
Gaia Collaboration, Brown, A. G. A., Vallenari, A., et al. 2018, A&A, 616, A1
Gilliland, R. L. 2005, Telescope Instrument Science Report 2005-02 (Baltimore, MD: STScI)
Gruyters, P., Nordlander, T., & Korn, A. J. 2014, A&A, 567, A72
Harrington, R. S., Dahn, C. C., Kallarakal, V. V., et al. 1993, AJ, 105, 1571
Haywood, J. W., Hegyi, D. J., & Gudehus, D. H. 1992, ApJ, 392, 172
Heintz, W. D. 1994, AJ, 108, 2338
Heintz, W. D., & Cantor, B. A. 1994, PASP, 106, 363
Heiter, U., Jofré, P., Gustafsson, B., et al. 2015, A&A, 582, A49
Holman, M. J., & Wiegert, P. A. 1999, AJ, 117, 621
Horch, E. P., Tokovinin, A., Weiss, S. A., et al. 2019, AJ, 157, 56
Horch, E. P., van Belle, G. T., Davidson, J. W., et al. 2015, AJ, 150, 151
Jao, W.-C., Nelan, E. P., Henry, T. J., et al. 2016, AJ, 152, 153
Jasniewicz, G., & Mayor, M. 1988, A&A, 203, 329
Jofré, P., Heiter, U., Soubiran, C., et al. 2014, A&A, 564, A133
Jofré, P., Heiter, U., Tucci Maia, M., et al. 2018, RNAAS, 2, 152
Johnson, H. L., & Morgan, W. W. 1953, ApJ, 117, 313
Karovicova, I., White, T. R., Nordlander, T., et al. 2018, MNRAS, 475, L81
Karovska, M., Nisenson, P., & Stachnik, R. V. 1986, AJ, 92, 898
Keenan, P. C., & Keller, G. 1953, ApJ, 117, 241
Korn, A. J., Grundahl, F., Richard, O., et al. 2007, ApJ, 671, 402
Lebreton, Y., Perrin, M.-N., Cayrel, R., et al. 1999, A&A, 350, 587
Lind, K., Bergemann, M., & Asplund, M. 2012, MNRAS, 427, 50
Lindegren, L., Hernandez, J., Bombrun, A., et al. 2018, A&A, 616, A2
Lippincott, S. L. 1981, ApJ, 248, 1053
Lippincott, S. L., & Wyckoff, S. 1964, AJ, 69, 471
Luck, R. E. 2017, AJ, 153, 21
Luck, R. E., & Heiter, U. 2005, AJ, 129, 1063
Mamajek, E. E., & Hillenbrand, L. A. 2008, ApJ, 687, 1264
Marino, A. F., Milone, A. P., Casagrande, L., et al. 2016, MNRAS, 459, 610
McCarthy, D. W., Jr. 1984, AJ, 89, 433
McCarthy, D. W., Jr., Hancock, T., & Freeman, J. 1993, AJ, 105, 652
Mermilliod, J. C. 1991, Catalogue of Homogeneous Means in the UBV System (Lausanne: Univ. de Lausanne)
Miczaika, G. 1940, AN, 270, 249
Nordlander, T., Korn, A. J., Richard, O., & Lind, K. 2012, ApJ, 753, 48
Nordström, B., Mayor, M., Andersen, J., et al. 2004, A&A, 418, 989
Önehag, A., Gustafsson, B., & Korn, A. 2014, A&A, 562, A102
Oort, J. H. 1926, PhDT, Leiden University
Pickles, A. J. 1998, PASP, 110, 863
Pierce, M. J., & Lavery, R. J. 1985, AJ, 90, 647
Planck Collaboration, Ade, P. A. R., Aghanim, N., et al. 2014, A&A, 571, A16
Richard, O., Michaud, G., Richer, J., et al. 2002, ApJ, 568, 979
Roman, N. G. 1955, ApJS, 2, 195
Russell, J. L., & Gatewood, G. D. 1984, PASP, 96, 429
Schlafly, E. F., & Finkbeiner, D. P. 2011, ApJ, 737, 103
Schlegel, D., Finkbeiner, D. P., & Davis, M. 1998, ApJ, 500, 525
Soubiran, C., Le Campion, J.-F., Brouillet, N., et al. 2016, A&A, 591, A118
Spite, F., & Spite, M. 1982, A&A, 115, 357
Thompson, I. B., Udalski, A., Dotter, A., et al. 2020, MNRAS, 492, 4254
Thygesen, A. O., Sbordone, L., Andrievsky, A., et al. 2018, A&A, 572, A108
van den Bos, W. H. 1964, in Astronomical Techniques, ed. W. A. Hiltner (Chicago, IL: Univ. Chicago Press), 537
van Leeuwen, F. 2007, A&A, 474, 653

VandenBerg, D. A., Bergbusch, P. A., Ferguson, J. W., & Edvardsson, B. 2014, ApJ, 794, 72
VandenBerg, D. A., Brogaard, K., Leaman, R., & Casagrande, L. 2013, ApJ, 775, 134, (VBLC13)
VandenBerg, D. A., Casagrande, L., & Stetson, P. B. 2010, AJ, 140, 1020
VandenBerg, D. A., Richard, O., Michaud, G., et al. 2002, ApJ, 571, 487
Wagman, N. E. 1961, AJ, 66, 433
Wagman, N. E., Daniel, Z., & Crissman, G. B. 1963, AJ, 68, 352
Wang, Y., Primas, F., Charbonnel, C., et al. 2017, A&A, 607, A135
Wehinger, P. A., & Wyckoff, S. 1966, AJ, 71, 185
White, T. R., Huber, D., Mann, A. W., et al. 2018, MNRAS, 477, 4403
Wickes, W. C. 1975, AJ, 80, 655
Wickes, W. C., & Dicke, R. H. 1974, AJ, 79, 1433
Worek, T. F., & Beardsley, W. R. 1977, ApJ, 217, 134